Master's dissertation

Master's degree in Automatic Control and Robotics (MUAR)

Integration of a redundant and collaborative robot in a teleoperated fetal surgical platform

Main report

Author: Tomàs Josep Pieras Morell

Director: Alícia Casals Gelpí

Codirector: Albert Hernansanz Prats

Date: June 2020

ETSEIB

Escola Tècnica Superior
d'Enginyeria Industrial de Barcelona

UPC

Abstract

Robotic Minimally Invasive Surgery is one of the surgical fields in which robotics is most extended. Minimally Invasive Surgery is used in fetal surgery for the correction of TTTS, among others pathologies. This technique has great complexity and long learning curves. To improve this surgery a robot-assisted TTTS surgery-oriented teleoperation platform was developed by the robotic division of the CREB-UPC.

This work integrates in this teleoperation system a set of improvements at a high-level control oriented to improve dexterity, safety and agility of the setup. This improvements are all implemented using a hierarchical based multi-task control. The control improvements are based on redundant and collaborative robots. This work studies the way to exploit the robot kinematic redundancy to increase the dexterity and reachability of the current teleoperation platform and optimize its space occupancy. Moreover, this work also studies collaborative strategies in the surgical workspace, to increase safety in human-robot interactions and optimize the platform preoperative set-up. The outcomes of this work will be integrated in the actual robotic teleoperated platform by replacing the current slave robot for a redundant and collaborative robot.

ETSEIB

Acknowledgements

I would like to express my gratitude to my supervisors Prof. Alícia Casals and Dr. Albert Hernansanz for they constant support and guide through this work. I would also like to particularly thank Narcís Sayols, for sharing with me his knowledge and helping through this project.

Contents

Abstract 1

Acknowledgements 3

List of figures 6

List of tables 9

List of acronyms 11

1 Introduction 13
- 1.1 HATTTS teleoperation plaform 15
- 1.2 Motivation 17
- 1.3 Objectives 19
- 1.4 State of the art 19
- 1.5 Document structure 23
- 1.6 Project planning 23

2 Multi-task control strategy exploiting redundancy in RMIS 25

3 Optimization of dexterity exploiting redundancy in RMIS 29
- 3.1 Dexterity of a robotic manipulator 30
- 3.2 Analysis of kinematic redundancy benefits on dexterity in RMIS 31
- 3.3 Dynamic manipulability optimization in RMIS 37

4 Human-robot interaction strategies for surgical robots 45
- 4.1 Obstacle avoidance strategy using robot redundancy 45
- 4.2 Compliant control strategy using null-space motion 52
- 4.3 Co-manipulation control strategy for manual operation. 57

5 Integration of a KUKA LightWeight Robot in HATTTS 61
- 5.1 Advantages of KUKA LightWeight Robot 4 61
- 5.2 Software integration 62

6 Project Budget 69

7 Project impact 71

8 Future Work 73

9 Conclusions 75

References 77

List of Figures

1 Transabdominal fetoscopy sets from Karl Storz used in FMIS. 13
2 Fetoscopic Laser Coagulation surgery. a) Representation of a monochorionic biamniotic twin gestation with TTTS. b) Representation of a monochorionic twin pair placenta with TTTS with different type of anastomosis circled. c) FLP intervention to ablate intertwin anastomoses. d) Representation the placenta with TTTS after FLP with coagulated points that divide the vascular system of the placenta. Adapted from [9]. 14
3 Schematic representation of the teleoperation platform. 16
4 Master console of the teleoperation platform. Main surgeon guides the fetoscope with the haptic device. In front, fetoscopic view. On the right, auxiliary screen with navigation map and interactive control buttons. 16
5 Slave module with current robot holding the fetoscope, Trocar Compensator and Laser Coagulation Module. A silicone placenta is placed on the Mistrainer platform (by SurgiTrainer). 17
6 Schematic of the communication between modules. 18
7 Robotic systems developed by Computer Motion. a) Automated endoscopic system for optimal laparoscope positioning (AESOP). b) ZEUS robotic laparoscopy system, with surgeon console and surgical station. 20
8 Robotic laparoscopy system da Vinci developed by Intuitive Surgical. 20
9 New emerging surgical technologies. a) Sensei X (Hansen Medical Inc., US). b) FreeHand 1.2 (FreeHand 2010 Ltd., UK). c) Single Port Orifice Robotic Technology (SPORT) Surgical System (Titan Medical Inc., Canada). d) NeoGuide Endoscopy System (NeoGuide Endoscopy System Inc, US). e) Senhance (TransEnterix, USA). 22
10 Matlab simulation of the robot-assisted FMIS environment. 24
11 Finite State Machine representation of the FLP surgical procedure. 25
12 Proposed control architecture with priority-based hierarchy using the null-space projection. Subtasks are designed to improve the dexterity and human-robot interaction of the teleoperated system. 27
13 Schematic representation of KUKA Lightweight robot. The external joint is labeled as θ_3. 29
14 Sampled FMIS workspace. Left: side view shows the division in Z axis. Right: top view shows the distribution in polar coordinates. 32
15 Example of various configurations with the same end effector pose for $q_3 = -\pi$, $q_3 = 0°$ and $q_3 = \pi$. 32
16 Different workspaces defined by the orientation of the trocar. (a) well-positioned workspace (b) ill-positioned workspace. 34
17 Reachability increment in workspace due to redundancy. Blue points represent positions in workspace reached by a non-redundant robot. Black points represent positions only reached with a redundant robot. 35
18 Manipulability value in the workspace. Robot base at $P_B = [0, 0, 0]$. (a) Manipulability value for non-redundant configurations (baseline values). (b) Maximum ratio between manipulability of redundant configurations and baseline values. . 35
19 Condition Number value in the workspace. Robot base at $P_B = [0, 0, 0]$. (a) CN value for non-redundant configurations (baseline values). (b) Minimum ratio between CN of redundant configurations and baseline values. 36

20 Isotropy value in the workspace. Robot base at $P_B = [0, 0, 0]$. (a) Isotropy index for non-redundant configuration. (b) Maximum isotropy ratio between redundant and non-redundant configurations. 37
21 Path defined for the dynamic optimization test. Initial position in green and final point in red. 38
22 Dynamic optimization with fixed boundaries policy. a) q_3 upper bound, yellow, and q_3 lower bound, in blue. b) q_3^*, in blue, and q_{3_0}, in red. c) Optimized configuration's manipulability normalized with w_0. d) Optimized configuration's isotropy normalized with Δ_0. 39
23 Dynamic optimization with linear boundaries policy. a) q_3 upper bound, yellow, and q_3 lower bound, in blue. b) q_3^*, in blue, and q_{3_0}, in red. c) Optimized configuration's manipulability normalized with w_0. d) Optimized configuration's isotropy normalized with Δ_0. 40
24 Dynamic optimization with radial boundaries policy. a) q_3 upper bound, yellow, and q_3 lower bound, in blue. b) q_3^*, in blue, and q_{3_0}, in red. c) Optimized configuration's manipulability normalized with w_0. d) Optimized configuration's isotropy normalized with Δ_0. 42
25 Example of optimized configuration with DOMERIM (highlighted) vs non-redundant configuration (ghost). a) Initial configuration. b-i) Sequence of consecutive motions. 43
26 Representation of the space occupancy in the surgery room. Some of the redundant joint configurations enter the medical staff space. 46
27 Representation of obstacle avoidance strategy exploiting redundancy and using potential repulsive fields and mass-spring-damped boundaries. 47
28 Results from the test of the obstacle-avoidance strategy exploiting redundancy. a) Displacement through the Y axis of the right lateral bound (red), left lateral bound (blue) and object (yellow) during the experiment duration. b) Repulsive force generated by the object (blue) and distance from the object to the left bound (red). 49
29 Changes in redundant joint value and boundaries during obstacle-avoidance experiment. The q_3 upper boundary is represented in red, the q_3 lower boundary in blue and the $q3$ value in yellow. 49
30 Results of the obstacle-avoidance experiment with dynamic manipulability optimization. a) Changes in redundant joint value and boundaries during obstacle-avoidance experiment. The q_3 upper boundary is represented in red, the q_3 lower boundary in blue and the $q3$ value in yellow. b) Manipulability ratio between the two experiments, where w_0 corresponds to the previous experiment manipulability. 50
31 Example of the collision-avoidance policy exploiting redundacy applied to a redundant robot performing a RMIS task. From a) to l), snapshots in chronological order. 51
32 Control structure the collaborative compliant control subtask. 52
33 Results from the joint compliance strategy exploiting redundancy. Left column: Compliance control with no stiffness. Right column: Compliance control with moderate stiffness. a,b) Force exerted over the robot arm (red) and variation of the joint value of q_3 (blue). c,d) Joint values for the time duration of the experiment, with dashed lines that marks the beginning and the end of the physical interaction. e,f) TCP position error in the Cartesian, with dashed lines that marks the beginning and the end of the physical interaction. 54

34 Compliant control exploiting null-space motion for human-robot interaction. Compliant control with no return (soft damper and no spring). Red sphere indicates physical contact. . . . 55
35 Compliant control exploiting null-space motion for human-robot interaction. Compliant control with return (soft damper and soft spring). Red sphere indicates physical contact. . . . 56
36 Control structure for the co-manipulation collaborative strategy . . . 58
37 Results from the test of the co-manipulation strategy. a) External forces and torques exerted on the tool tip. b) Joint values. . . . 58
38 Co-manipulation control for physical guidance of the robot. The red arrow indicates the force vector exerted on the end effector. . . . 59
39 The Kuka LightWeight Robot 4 with KUKA Robot Controller (KRC) and KUKA control panel (KCP) . . . 61
40 Diagram of FRI control architecture. Figure source from [45]. . . . 62
41 State machine for FRI monitor and command mode. Figure source from [46]. . . . 63
42 State machine of the data transfer quality and the allowed modes. Figure source from [46]. . . . 63
43 Graphic user interface simulating the KUKA LWR teach pendant using FRI. Available at the laboratory prior to this project. . . . 64
44 Integration of the KUKA LWR4 into the control architecture of the HATTTS system using a intermediary abstraction layer . . . 64
45 Graphic user interface for the interpreter module. . . . 65
46 Finite State Machine representation of the interpreter module. . . . 67

List of Tables

1 Comparison of main features of KUKA LWR4 and Staübli RX60B 62
2 Project budget. 69

List of acronyms

MIS	Minimally Invasive Surgery
RMIS	Robotic Minimally Invasive Surgery
RAMIS	Robotic-Assisted Minimally Invasive Surgery
FMIS	Minimally Invasive Fetal Surgery
TTTS	Twin-to-Twin Transfusion Syndrome
FLP	Fetoscopic Laser Photocoagulation
YAG	Neodymium-yttrium Aluminium Garnet
DoF	Degrees of Freedom
GRINS	Research Group on Intelligent Robotics and Systems
CREB-UPC	Center of Research in Biomedical Engineering at Universitat Politècnica de Catalunya
HATTTS	Herramientas avanzadas para la cirugía fetal en TTTS
POI	Point of Interest
LWR	Lightweight Robot
RCM	Remote Center of Motion
FSM	Finite States Machine
OSF	Operational Space Formulation
IK	Inverse Kinematics
FK	Forward Kinematics
DOMERIM	Dynamic Optimization of Manipulability Exploiting Redundancy in Incremental Motion
HRI	Human-Robot Interaction
DLR	German Aerospace Center (Deutsche Zentrum für Luft- und Raumfahrt e.V.)
KRC	KUKA Robot Controller
KRL	KUKA Robot Language
FRI	Fast Research Interface

1 Introduction

Robotic-assisted surgery takes advantage of robotic systems to allow surgeons to perform complex procedures with more precision and control than conventional surgery, improving patient safety and surgery outcomes. The most extended use of robotics in surgery is in the fields of orthopedics, neurology, medical imaging and minimally invasive surgery (MIS). Robotic Minimally Invasive Surgery (RMIS) is performed through small incisions as opposed to conventional open surgery. The main advantages of minimally invasive surgery, compared to open surgery, are the reduction of blood loss, quicker recovery after the surgery, smaller scars and fewer post-operatory complications [1]-[4]. However, MIS has also some drawbacks deriving from the laparoscopic tools and the indirect vision: loss of dexterity, reduction from 7 DoF (human wrist in open surgery) to 4 DoF, dissociation of visual perception from the manipulation, lack of tactile feedback, etc. RMIS eliminates the main disadvantages of MIS with technical features: Hand tremor filtering, motion scaling, enhance of visual perception, optimized ergonomics, virtual fixtures, etc.

Among the different applications of MIS, fetal surgery or intrauterine surgery allows a minimally invasive approach to the treatment of congenital defects or gestation complications in the fetus, placenta or umbilical cord. This surgical technique is a novel approach that allows the correction or minimization of, among others, the effects of Twin-to-Twin Transfusion Syndrome (TTTS), thoracic effusions (intrathoracic shunt placement), diaphragmatic hernias (temporary placement of a trachea ball), etc [5]-[6]. Without this approach, these syndromes could not be corrected, and the life of the fetus would be at risk.

A minimally invasive approach is less harmful than its conventional counterpart in fetal surgery and allows the preservation of the tissues of the amniotic sac. A premature rupture of the amniotic sac can carry a high risk of maternal or fetal infection, placental problems and premature birth. However, Minimally Invasive Fetal Surgery (FMIS) is a highly demanding surgery at the technical level, requiring great surgical skills and long learning curves. FMIS uses special tools called fetoscopes, 20-30 mm long endoscopes with a diameter that ranges between 1.2-3.8 mm. Fetoscopes have an image transmission system from the tip to the back, where a camera is connected (generally with a rod lens system or optical fibers), and working canals (through the tool or the protective sheaths) to insert graspers, laser optic fiber or liquid infiltrations (fig. 1).

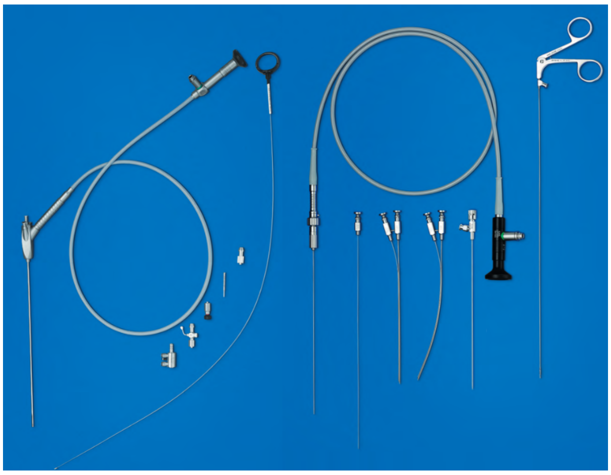

Figure 1: Transabdominal fetoscopy sets from Karl Storz used in FMIS.

One of the surgeries in which the use of FMIS has been most extended is Fetoscopic Laser Photocoagulation (FLP), a laser therapy used for the correction of the Twin-to-Twin Transfusion Syndrome. TTTS is a severe complication in twins pregnancies where fetuses share a single placenta (monochorionic twins) and occurs when there is communication between the fetuses blood systems. The inter-twin vessel communications are called anastomosis. The syndrome can cause a chronic blood transfer from one fetus, the donor, to the other fetus, the recipient, which leads to cardiovascular disturbances and results in their death in 90% of cases. Statistical studies estimate that TTTS affects 10-15% of all monochorionic twins, about 1-3 out of 10,000 births (1 in 2000). Other multiple complications that may result from TTTS: intrauterine infra development of the donor fetus, cardiomyopathies in the receiving fetus, morbidity in neurodevelopment, etc. The survival rates of at least one twin after the surgery correction ranges from 76% to 88%. However, there is still a 13 to 17% risk of long-term neurodevelopmental impairment [7].

The goal of FLP intervention is to ablate all the intertwin anastomoses to make independent the twins' vascular systems from each other [8]. The technique for laser therapy involves the following sequence of steps. First, the fetoscope is inserted to obtain direct view of the placenta. Next, the umbilical cords of both twins are identified to help locate the equator. The equator is the region equidistant to the two umbilical cords and generally anastomoses are concentrated there. Having defined the equator, the surgeon proceeds to inspect the region in order to identify the anastomosis. Once the inspection is completed, proceeds to coagulate the anastomosis with a high power laser (YAG or diode) introduced through the fetoscope. A final inspection is done to review the quality of ablations and find any unnoticed anastomosis before extracting the fetoscope. Figure 2 shows a representation of a twin gestation with TTTS and FLP correction.

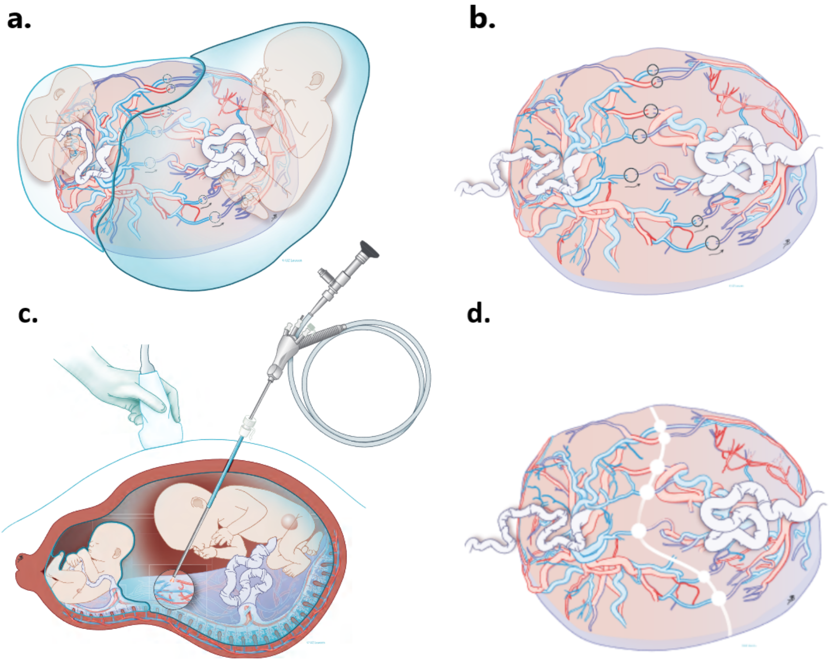

Figure 2: Fetoscopic Laser Coagulation surgery. a) Representation of a monochorionic biamniotic twin gestation with TTTS. b) Representation of a monochorionic twin pair placenta with TTTS with different type of anastomosis circled. c) FLP intervention to ablate intertwin anastomoses. d) Representation the placenta with TTTS after FLP with coagulated points that divide the vascular system of the placenta. Adapted from [9].

In order to apply the benefits of RMIS to fetal surgery, a recently finished project (2016-2019) for high precision new technologies in medicine and fetal surgery established a framework of cooperation between medical and robotic research groups. The medical team was formed by the Fetal Medicine Research center from BCNatal, a consortium formed by the SJD Barcelona Children's Hospital and Hospital Clínic. The robotic team was formed by part of the Research Group on Intelligent Robotics and Systems (GRINS), a section of the Center of Research in Biomedical Engineering at Universitat Politècnica de Catalunya (CREB-UPC). This project was financed by the private foundation Fundació Cellex. As a result of this collaboration, a robot-assisted TTTS surgery-oriented teleoperation platform (HATTTS) was developed. HATTTS comes from the project title in Spanish: *Herramientas Avanzadas para la cirugía fetal en TTTS*. This teleoperation platform has a master console, from where the surgeon commands the movement of the fetoscope using a 6 DoF haptic device, and a slave station, which has a 6 DoF robot with the fetoscope as end effector. A further technical description of the system is explained in 1.1. The system has been tested in an experimental environment, where several surgeons performed a simulation of the TTTS surgery procedure to prove the viability of the proposed solution. The medical team validated the usability of the system and acknowledged the improvement in precision, perception, control and data registration over the conventional manual surgery.

The objective of this work is to define a control strategy for a redundant and collaborative robot that optimize the performance of a teleoperated RMIS procedure. A multi-task control strategy exploiting the redundancy of the robot is proposed, which allows the performance of subtasks simultaneously to the main task without interfering. Using the redundancy and collaborative capabilities of the robot, various subtasks are developed to enhance the capabilities of the robot-assisted surgery in terms of dexterity and human-robot interaction (e.g. dexterity optimization, joint compliant control, obstacle-avoidance). The control strategy proposed with new features that enhance the robot performance will be integrated in the HATTTS system, which at the start of this work relies on a 6 DoF manipulator. The integration of a KUKA LightWeight Robot 4, which is a redundant and collaborative robot, will allow the implementation of the developed work to the HATTTS system.

1.1 HATTTS teleoperation plaform

The teleoperation platform has been designed for single tool minimally invasive fetal surgery, following the FLP surgical technique. The modular arquitecture opens the possibility to adapt to new surgeries. The first surgical technique addressed is Fetal Laser Photocoagulation for TTTS correction. The teleoperation platform offers different solutions to the surgeons oriented to improve the detected critical aspects. The teleoperation platform is divided into three main modules: Master Console, Slave Station and a centralized control module (fig. 3).

The interaction between the surgeons and the teleoperation platform is conducted using an interactive master console. The designed master console is composed of an interactive and modular Graphic User Interface (GUI), a 6DoF haptic device (Touch haptic device by 3D Systems) and four pedals for auxiliary and safety actions (e.g. emergency exit using the direction of the tool to avoid any damage of the patient). The haptic device guides the fetoscope considering the kinematic restrictions imposed by the Remote Center of Motion (RCM), also called the fulcrum point. The surgeons guide the tool tip, compensating the current movement paradigm (inverse movements for camera navigation) forced by the RCM. The GUI is oriented to provide the surgeons with the required information to perform the surgery like the fetoscopy camera view, a navigation map, interactive marking of anastomoses with type labels, Points of Interest (POI)

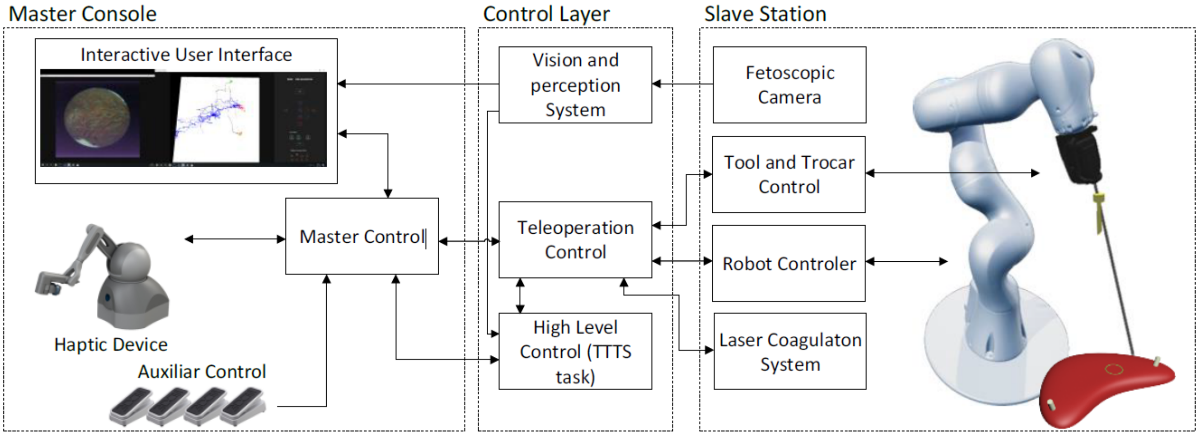
Master Console
Control Layer
Slave Station
Interactive User Interface
Vision and perception System
Fetoscopic Camera
Tool and Trocar Control
Master Control
Teleoperation Control
Robot Controler
Haptic Device
High Level Control (TTTS task)
Laser Coagulaton System
Auxiliar Control

Figure 3: Schematic representation of the teleoperation platform.

historic information (identified, coagulated, revised), etc. The teleoperation control also offers other software aiding tools oriented to the surgical task in execution, such as automatic navigation to POIs, automatic laser extraction/retraction, activate safety planes and data registration. Figure 4 shows the master console used during the experimental phase, where surgeons with different experience test manual and robotic platforms to compare the obtained performance.

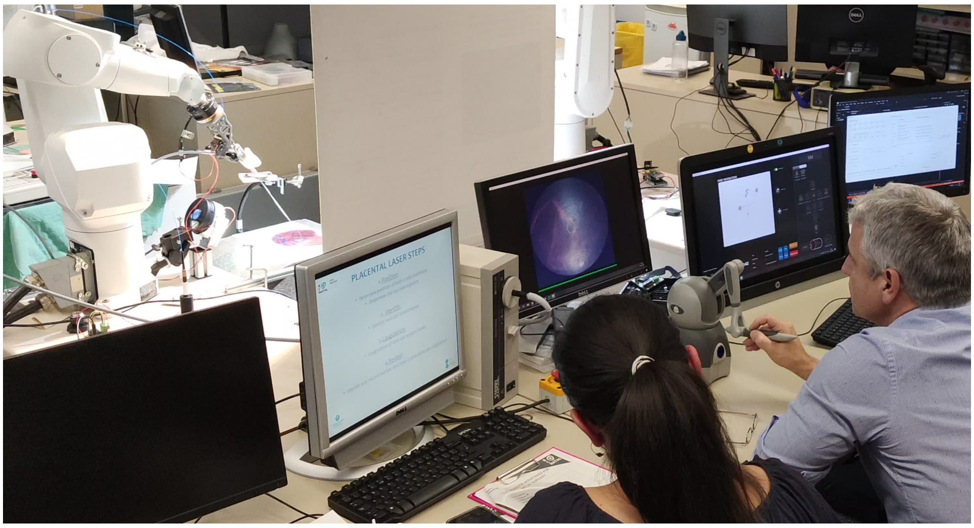
PLACENTAL LASER STEPS

Figure 4: Master console of the teleoperation platform. Main surgeon guides the fetoscope with the haptic device. In front, fetoscopic view. On the right, auxiliary screen with navigation map and interactive control buttons.

The slave module of the system is composed of a robot arm with a specific holder that fixes the fetoscope to the end effector, the Laser Coagulation System and the Trocar Compensator. Currently, the used robot is a 6 DoF Staübli Rx60. The developed Laser Coagulation Module (LsrC) gives the control of the fiber extraction and retraction to the main surgeon, which normally requires an auxiliary surgeon only for the fiber handling, increasing the precision and repeatability of the coagulation process and decreasing the potential collisions between fiber and placenta. The developed Trocar Compensator Module (TrC) is a device that controls the trocar's insertion depth. The friction between fetoscope and trocar causes undesired depth variation of the trocar inside the uterus. This can cause a tissue rupture or even an accidental trocar extraction, which would require to realize a new puncture increasing the risk of amniotic sac membranes break. In manual surgery, the main surgeon holds the trocar with the non dominant hand fixing the depth. This decreases the ergonomy of the surgeon and, consequently, precision. TrC actively compensates the fetoscope depth variations using a linear actuator. TrC is attached to the link between robot and fetoscope and fixes the trocar head, ensuring the alignment between trocar and fetoscope. Figure 5 shows the current slave experimental set-up.

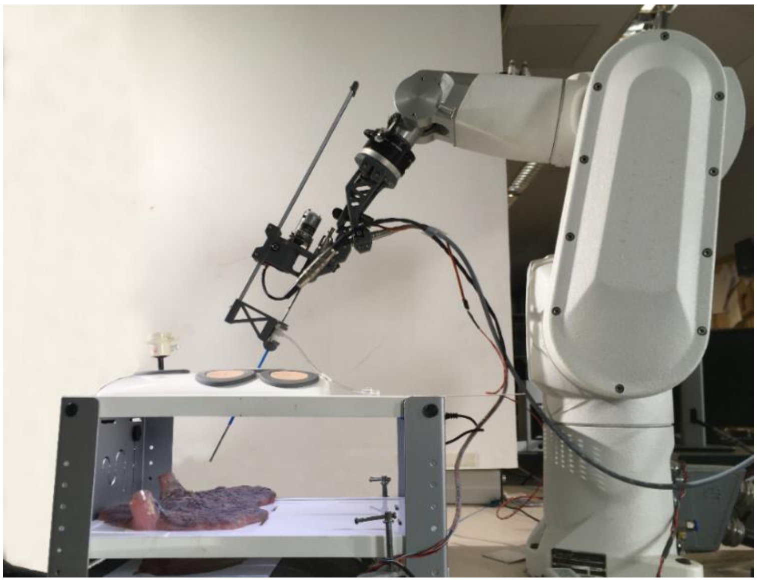

Figure 5: Slave module with current robot holding the fetoscope, Trocar Compensator and Laser Coagulation Module. A silicone placenta is placed on the Mistrainer platform (by SurgiTrainer).

The teleoperation platform uses a centralized control model to generate robot trajectories based on the surgical task: automatic or manual navigation and emergency tool exit. Trajectories computation also contemplate risk evaluation, motion compensation and fine location. The entire communication flow of the master and slave modules pass through the central control module, which communicates with all modules and submodules. Communications are client-server based using TCP-IP sockets where the central system acts as a client and the rest as servers. Figure 6 shows an schematic of the communications of the system.

1.2 Motivation

The fetal surgery teleoperated system HATTTS has obtained face validity from the BCNatal Research Center team, one of the leading research centers in fetal medicine. The platform was tested by 14 surgeons in a two session experiment, where they compared the HATTTS system to manual FLP. The vision of the project HATTTS was to contribute to the medical field with an robotic-assisted system that reduces the complexity of the surgery and the required skills, thus extending the accessibility of FLP through hospitals around the world. To reach this development stage the system has to be safe to use in surgery, both for the patient and for the medical staff involved in the procedure. For this purpose this project will change the current slave robot, a 6 DoF (STaübli RX60b), for a redundant collaborative robot (KUKA LWR 4) and use its added capabilities to enhance the system in dexterity and safety. The idea of using this robot answers three needs raised during the previous project.

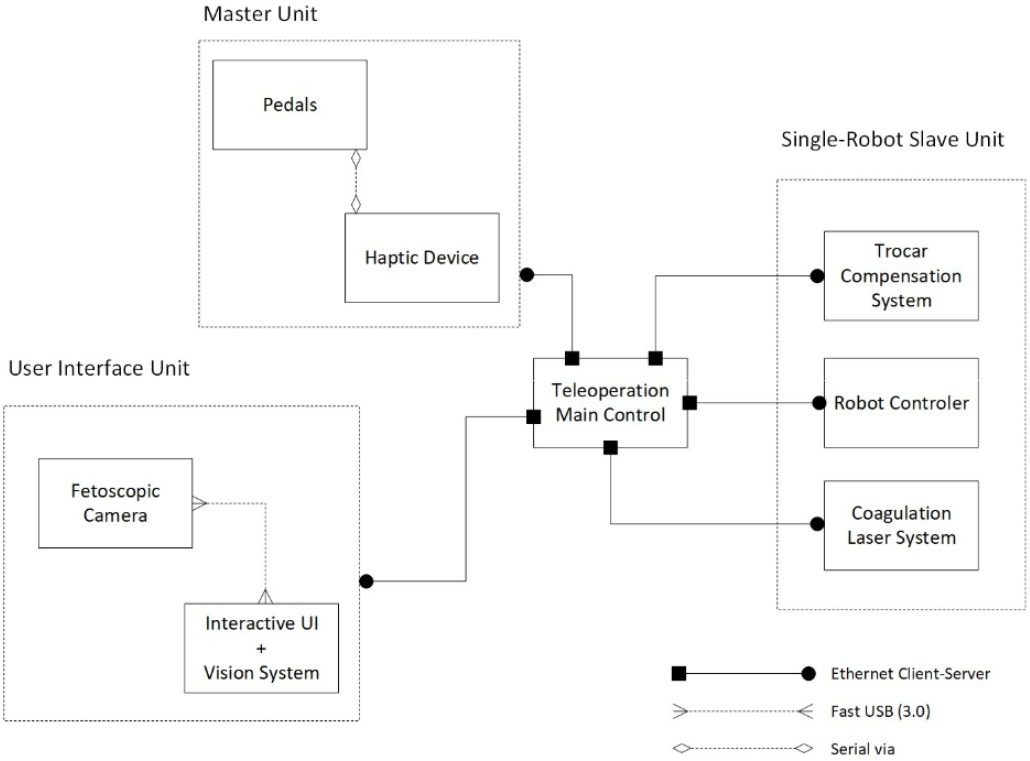
Master Unit
Pedals
Haptic Device
Single-Robot Slave Unit
Trocar Compensation System
Robot Controler
Coagulation Laser System
Teleoperation Main Control
User Interface Unit
Fetoscopic Camera
Interactive UI + Vision System
Ethernet Client-Server
Fast USB (3.0)
Serial via

Figure 6: Schematic of the communication between modules.

First, the slave robot kinematics are highly restricted due to the RCM. In addition, the robot is restricted to a fixed configuration (left handed, elbow up, wrist no flip) to prevent uncontrolled movements during the procedure. This leads to a reduced dexterity, operative workspace, and a restricted robot positioning for the surgery. The kinematic redundancy of the KUKA LWR allow null-space motion. Null-space motion allows changes in the configuration of the robot that do not modify the position of the end effector. Null-space motion can be used to improve the dexterity of the robot, to free space in the robot surroundings required for the auxiliary surgeon with the ultrasound probe or other medical staff or react against a collision with compliant behaviour.

Second, this robot is endowed with torque sensors in each joint which can measure external forces exerted onto the robot. These sensors facilitate the implementation of collaborative strategies to enhance human-robot interaction. Compliant control can handle collisions or physical interaction between the robot and the medical staff, making the surroundings of the robot safe to be occupied. In addition, co-manipulation would optimize the set-up of the robot using physical guidance. The actual set-up procedure is cumbersome and causes a great waste of time increasing the economic cost of the surgery.

Third, this robot complies with current regulations and can enter into an operating room therefore the integration of this robot in the system will allow the project to advance towards new experiments. Moreover, there is a recent version of this robot, the KUKA LBR Med, designed specifically for medical applications with same geometry and kinematic configuration as the KUKA LWR 4. The KUKA LBR Med is certified for integration into a medical product, based on the internationally recognized "ECEE CB Scheme", and complies with international standards IEC 60601-1 and IEC 62304.

1.3 Objectives

The main objective of this project is to develop a control strategy for RMIS that, in addition to focus on the surgical task, implements a set of features that increase the capabilities of the teleoperated system in terms of dexterity and human-robot interaction. The desired features are the optimization of dexterity, a strategy to free up part of the shared workspace for the medical staff, a compliant behaviour in case of human-robot physical interaction and a co-manipulation control to manually steer the robot in a desired trajectory. In order to integrate the features developed in this work into the HATTTS system, the actual robot in the slave module will be replaced for a new redundant and collaborative robot. This objective can be split into the following tasks:

1. Define a multi-task control strategy for RMIS.
2. Study the kinematic redundancy's benefits on dexterity.
3. Develop an algorithm for optimization of manipulability by means of redundancy.
4. Develop an obstacle avoidance strategy exploiting redundancy.
5. Design of collaborative control strategies in shared surgical scenarios.
6. Integrate a redundant and collaborative robot in a robot-assisted fetoscopy teleoperation system.

1.4 State of the art

This section reviews the state of the art of robotic in surgery. The explanation will begin with a brief historical overview of the introduction of robotic in the medical field, then it will focus on the current robotic technologies for Minimally Invasive Surgery. The section will end with a quick review of the literature in robotic technologies for fetal minimally invasive surgery. For further information the reader can consult [10] for a overview of medical robotics and [11] for a review of emerging technologies in surgical robotics.

Robotics have been used in the medical field for more than 30 years, and its use continues expanding with novel medical applications. The first use of robotics in surgery was in 1985, where a PUMA robot was used to assist a neurosurgical biopsy [12]. In 1988, the robotic surgical system *ROBODOC* was used to precisely drill the femoral head to insert the hip replacement prosthesis [13]. In the same year, at Imperial College in London, a group of researchers performed the first robot-assisted urology surgery using a PUMA robot [14], which lead to the development of the *PROBOT* system [15]. Neurosurgery and orthopedics where the first fields to introduce robot-assisted surgical procedures due to the application in non-deformable tissues like bones. Those systems where preprogrammed for each patient and based on fixed fiducial markers.

The deformation of soft tissues like the organs, makes the use of preprogrammed robots very challenging. Researchers found that teleoperation surgical platforms are the best robotic solution for surgeries on internal deformable organs (e.g. abdominal region). Through telemanipulation, the surgeon operates the robot from distance. Laparoscopy quickly adopted the robotic teleoperation solution. In 1993, Yulyn Wang founded the Computer Motion company, and developed the first robotic device for use in endoscopic surgery (fig. 7a) approved by the

US Food and Drug Administration (FDA). The Automated Endoscopic System for Optimal Positioning (AESOP) was used to control the camera in a laparoscopic surgery [16]. Years later, the same company developed a more complex robotic system for laparoscopy called ZEUS (fig. 7b). The Zeus system had three teleoperated robotic arms commanded by the surgeon from a console. One arm controlled the endoscope, while the other two could hold a variety of surgical instruments such as graspers or scissors.

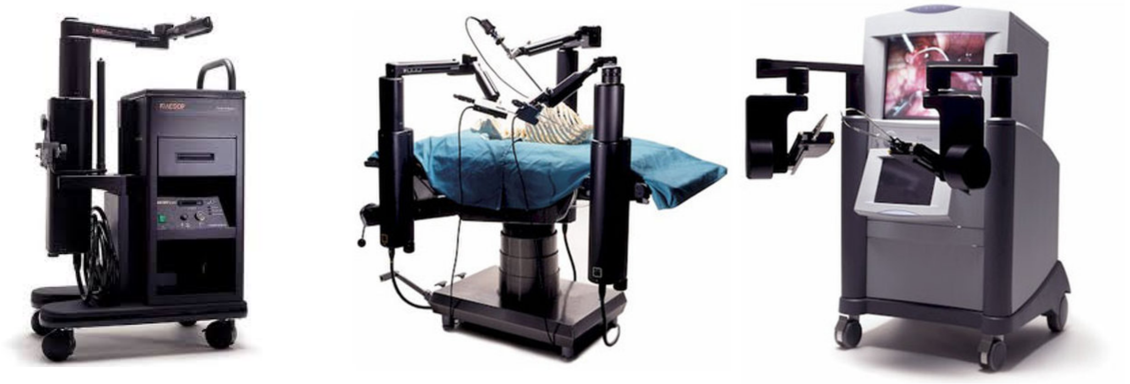

(a)

(b)

Figure 7: Robotic systems developed by Computer Motion. a) Automated endoscopic system for optimal laparoscope positioning (AESOP). b) ZEUS robotic laparoscopy system, with surgeon console and surgical station.

Also during the 1990s, parallel to the development of the ZEUS system, a Californian company named Intuitive Surgical developed the da Vinci, a robotic surgical system for general laparoscopy [17]. The da Vinci followed the same architecture than ZEUS, with a master console for the main surgeon and a slave station with two robotic operating arms and one camera holder. The operating arms of the da Vinci offered 7 DoF, replicating the surgeon's movements, and can hold a wide variety of surgical tools. The following versions of da Vinci incremented the number of operative arms up to four. Last da Vinci versions include the possiblity of single port surgery (fig. 8).

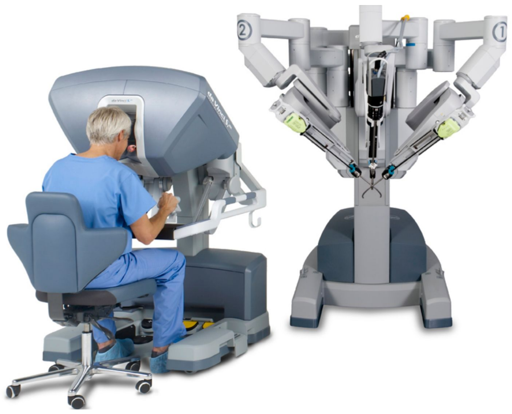

Figure 8: Robotic laparoscopy system da Vinci developed by Intuitive Surgical.

Both robotic surgery systems were approved by the FDA and were used in digestive, oncologic, cardiac, gynecologic and urologic surgeries. The satisfactory performance of these two systems introduced the computer-enhanced robotic surgery into the general surgical practice [18]. In

2003 Computer Motion was merged into Intuitive Surgical and Zeus was phased out in favor of da Vinci. Da Vinci is currently the most widespread robotic surgical system for laparoscopy, with more than 5.000 units distributed in 67 countries. According to the company's data, more than 7 millions da Vinci procedures were completed by 2019, 15% through the last year.

Although the most popular surgical robotic system is the da Vinci, the trend in robot-assisted minimally invasive surgery has increased the number of current available surgical robotic technologies. Some of the popular new robotic surgical systems are the Sensei X (fig. 9a), for robot-assisted cardiac catheter insertion, the FreeHand (fig. 9b), a next generation endoscope holder, the Single Port Orifice Robotic Technology (SPORT) Surgical System (fig. 9c), a console-based platform for laparoendoscopic single site, the NeoGuide Endoscopy System (fig. 9d), for computed-aided colonoscopy, and the Senhance (fig. 9e), a robotic platform for general laparoscopy. At local level, RobSurgical, a spin-off from the Universitat Politècnica de Catalunya (UPC) and the Institute for Bioengineering of Catalonia (IBEC), is also developing a multi-arm laparoscopic robot with passive joints between robot arms and tools to minimize tool forces exerted over the abdominal wall.

Despite the uprising popularity in robot-assisted surgery, the use of robotic techniques to fetal surgery has been poor. Commercial robotic surgical systems, like da Vinci, are not adequate due to the small size of the surgical space in comparison to their tool sizes. Researchers have focused in developing robotic technologies specifically designed for fetal surgery. Some of the current robotic fetal surgery technologies are a fetal blood sampling robot[19], a microfabricated instrument for haptic tissue recognition [20], a robotic manipulator for intrauterine fetal surgery for tracheal occlusion [21] and a fetoscopic instrument with a decoupled tip of 2 DoF for FLP surgery [22]. Moreover, due to the poor visibility in intrauterine surgery (low quality image, liquid environment with no light, thin optic diameters) part of the developed work focus on computer vision techniques to enhance visual perception. Tracking of the vascular structure and other features can be used to generate a placental panoramic view through fetoscopic image reconstruction [23]-[24]. In [25], besides the mosaicking of the placenta, vessel tracking is used to locally guide a robot with enough accuracy.

(a) Sensei X (b) FreeHand

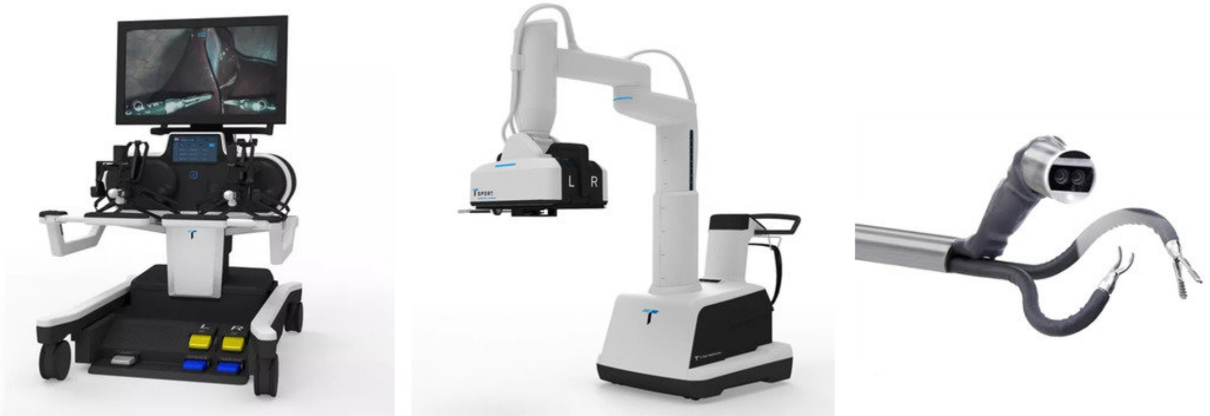

(c) SPORT

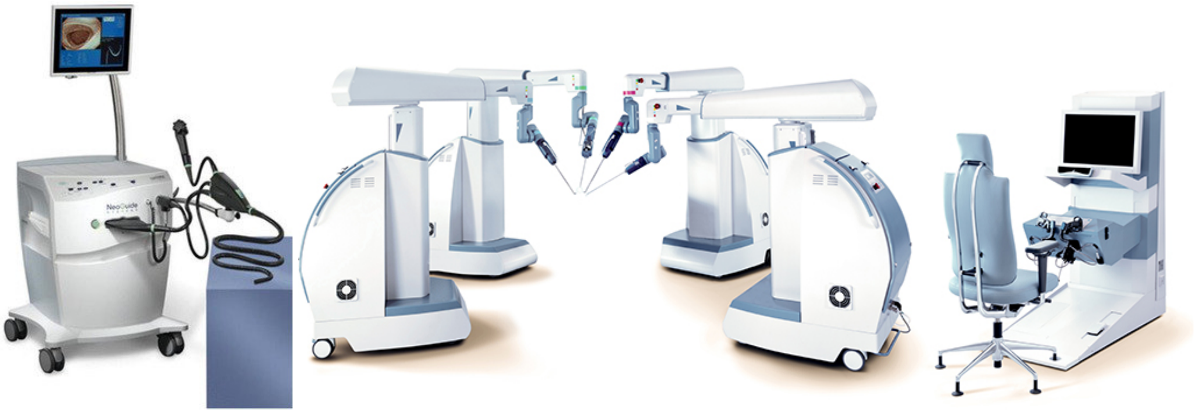

(d) NeoGuide (e) Senhance

Figure 9: New emerging surgical technologies. a) Sensei X (Hansen Medical Inc., US). b) FreeHand 1.2 (FreeHand 2010 Ltd., UK). c) Single Port Orifice Robotic Technology (SPORT) Surgical System (Titan Medical Inc., Canada). d) NeoGuide Endoscopy System (NeoGuide Endoscopy System Inc, US). e) Senhance (TransEnterix, USA).

1.5 Document structure

This introductory chapter covers the project context and the proposed objectives. Chapter 2 introduces a multi-task control strategy for a redundant robot in the FLP procedure. The chapter presents additional control strategies defined as a sub-task of the system. The proposed subtasks are based on redundancy and collaborative techniques. Chapter 3 explores the improvement of dexterity by means of redundancy. It starts with an introduction to redundant manipulators and dexterity. Then, presents a study of the kinematic redundancy benefits to maximize dexterity. Next, the section describes an online manipulability optimization algorithm using a redundant robot. Chapter 4 is dedicated to the development of human-robot interaction strategies. This section starts with an obstacle avoidance strategy exploiting redundancy. Following, a compliant control for collision reaction using null-space motion is proposed. Furthermore, the design of a co-manipulation strategy for physical guidance is discussed. Chapter 5 explains the integration of a KUKA LWR 4 into the HATTTS platform to implement the developed functionalities. In chapter 6 the cost of this project is detailed. Chapter 7 presents a brief socioeconomic and environmental impact of the project. Chapter 8 proposes the future work for the continuity of this project. Chapter 9 presents the conclusions of this project.

1.6 Project planning

This section explains the project planning and work structure. The first task of this work was the development of the software layers necessary for high-level control and integration of the robot within the HATTTS system (Chapter 5). The second task addressed by the project has been the development of manipulability optimization strategies exploiting the redundant robot capabilities (chapter 3). The corresponding chapter introduces the concepts of different robotic dexterity evaluation indices and the benefits of redundancy in RMIS. The chapter concludes with a review of the developed strategies for dynamic manipulability optimization and shows several studies that illustrate the usefulness of the proposed approximation. The third phase of the project has been based on the development of human-robot interaction strategies focused on surgical robotic applications (chapter 4).

The completion of the first task allowed the implementation and test, on the real system, of the control strategies developed in this work. However, the test and validation of the proposed controls on the real system has been not possible given the lockdown and laboratory closure imposed by the situation caused by the Covid-19. To overcome with this situation, the control strategies have been developed, tested and validated through simulation using Matlab.

The 2019 Matlab Robotic System Toolbox offers a set of tools and algorithms for designing, simulating and testing robotic manipulators. The simulations have been realized with the kinematic model of a KUKA LBR iiwa, a more recent version of the KUKA LWR 4 that preserves the same kinematic configuration. To simulate the FMIS, a fetoscope shaped body is attached to the robot end-effector and a RCM constrain is defined at the trocar position. The surgical workspace is defined as a cone with vertex on the trocar position (fig. 10).

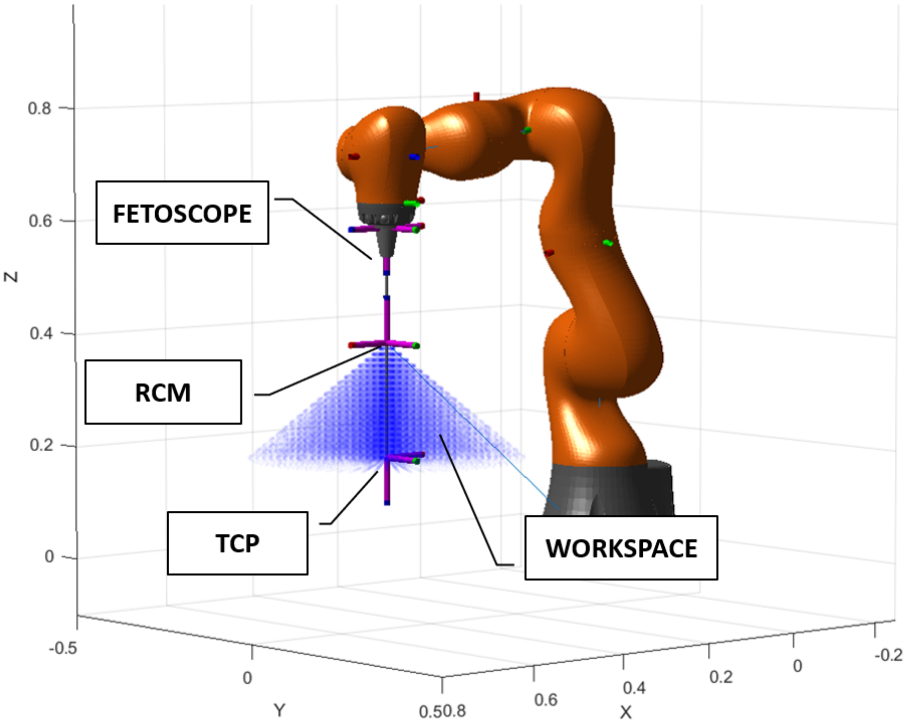
FETOSCOPE
RCM
TCP
WORKSPACE
Z
0.8
0.6
0.4
0.2
0
-0.5
0
Y
0.5
0.8
0.6
0.4
X
0.2
0
-0.2

Figure 10: Matlab simulation of the robot-assisted FMIS environment.

2 Multi-task control strategy exploiting redundancy in RMIS

In order to enhance the HATTTS system performance, the implementation of any additional control strategy must not interfere with the development of the surgical procedure. Currently, HATTS teleoperation platform is equipped with a 6DoF serial robot which does not allow the implementation of multiple control strategies. This chapter introduces a multi-task control strategy using a redundant and collaborative robot, which allows the implementation of multiple control schemes for the FLP procedure.

The FLP surgery can be described with a Finite State Machine (FSM). This approximation enables a better understanding, formal description and identification of the parameters (e.g. risks, most challenging or time consuming actions) that define the control strategies to improve the surgery performance and patient safety. Figure 11 shows the proposed division of the surgery in the phases pre-operatory setup, POI location, coagulation, revision, post-operatory setup and a emergency state where the tool is partially or complete extracted. This division has been reviewed and approved by the medical team involved in the project. Each phase presents specific requirements in terms of robot guidance modes and multi-task control schemes.

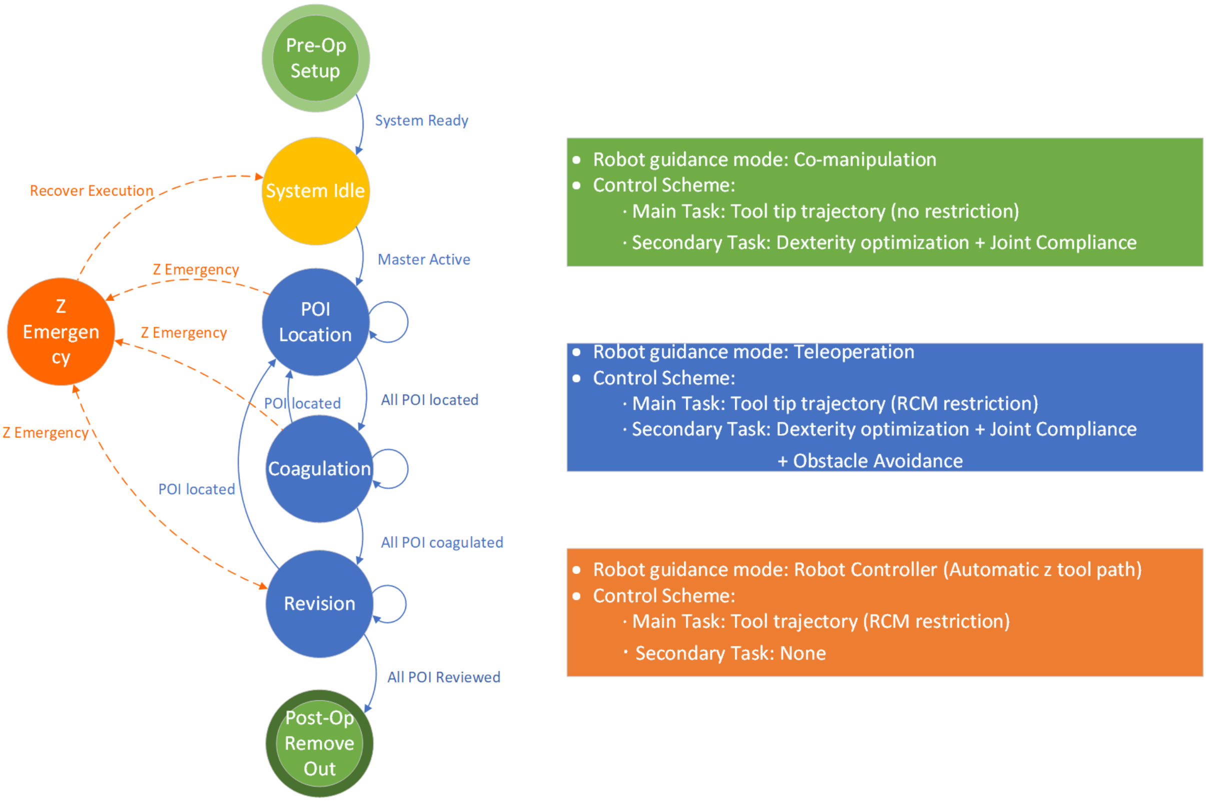
Pre-Op Setup
System Ready
System Idle
Recover Execution
Master Active
Z Emergency
Z Emergency
POI Location
Z Emergency
POI located
All POI located
Coagulation
POI located
All POI coagulated
Revision
All POI Reviewed
Post-Op Remove Out
Robot guidance mode: Co-manipulation
Control Scheme:
· Main Task: Tool tip trajectory (no restriction)
· Secondary Task: Dexterity optimization + Joint Compliance
Robot guidance mode: Teleoperation
Control Scheme:
· Main Task: Tool tip trajectory (RCM restriction)
· Secondary Task: Dexterity optimization + Joint Compliance + Obstacle Avoidance
Robot guidance mode: Robot Controller (Automatic z tool path)
Control Scheme:
· Main Task: Tool trajectory (RCM restriction)
· Secondary Task: None

Figure 11: Finite State Machine representation of the FLP surgical procedure.

Two robot guidance modes are proposed: telemanipulation and co-manipulation. Telemanipulation allows the control of the tool tip trajectory from a remote master device. The main surgeon focus on the control of the tool tip to gain precision and control during the surgery. Co-manipulation is a collaborative strategy that allows the control of the robot from physical interaction. The surgeon moves the robot end effector by means of manual guidance (direct physical interaction between surgeon and robot arm). The robot allows this two control modes as it is integrated in a teleoperation system, thus can be telemanipulated, and has integrated torque sensors in the joints, thus allowing co-manipulation.

The additional control strategies, labeled in figure 11 as secondary tasks, are additional features desired for the teleoperation system. The dexterity optimization maximizes the manipulabitily of the robot for the surgical task evaluating multiple redundant configurations. The collision-avoidance strategy exploits the robot redundancy to free occupancy space when a surgeon or nurse approximates the robot, reducing the collision probability. The joint compliance control provides a docile arm behaviour when there is a physical interaction between human and robot. The joint compliance can be used to control the reaction of the robot in a collision and to allow the surgeon to modify the arm configuration by hand.

These control strategies will be implemented into the HATTTS high level robot control system to be used during the surgery. The use of the additional control strategies will be regulated according to the ongoing phase of the surgery, as proposed in figure 11. For example, in the POI location phase, where a sonographer helps to locate the placenta and the fetuses, the obstacle-avoidance is used to prevent collisions whereas its use has no sense during the co-manipulation mode, as the surgeon is in direct contact with the robot.

Redundant manipulators offer infinite configurations when solving the IK problem in the task space. Kinematic redundacy leads to possibility of exploiting redundancy to optimize certain criteria in the form of subtasks. Considering a multi-task approach, each operational space objective $task_i$ (e.g. end effector trajectory, joint movements minimization, dexterity optimization...) contributes to the dynamics of the robot. The tasks contribution can be weighted or prioritized to establish a control hierarchy. For redundant manipulators, the most well-known control framework in task space is the Operational Space Formulation (OSF) developed by [26]. In OSF, the linear dynamics of the main task are decoupled allowing the control of various tasks simultaneously. In [27]-[28] and, more recently, in [29], a multi-task control with a priority-based hierarchy for redundant manipulators is proposed, using the null-space projection of the Jacobian matrix. Using this approach, tasks with lower priority can be performed utilizing redundancy of tasks with higher priority, but with the guarantee that a task will not be perturbed by another with lower priority. The null-space of a redundant robot's Jacobian matrix ($J_r^{m \times n}$) is a subset of that matrix such that

$$N = \{v \in R^{n \times n} \mid J_r v = 0\} \tag{2.1}$$

Therefore, the contribution of a task executed in the null-space ($\dot{q}_N$) to the end effector velocity ($\dot{X}_{EE}$) is

$$\dot{X}_{EE}\Big|_{task_N} = N\dot{q}_N = 0 \;\; \forall \dot{q}_N \tag{2.2}$$

A generalized framework for control of redundant manipulators in RMIS, proposed in [29], defines a strict priority task hierarchy approach. In this generalized framework, the main task is defined as the control of the tool-tip trajectory. Secondary tasks, performed in the null-space, allow the addition of features (e.g. joint compliance, dexterity optimization, motion economy) without altering the critical main task. Following this framework, in this work a redundant manipulator is used in the HATTTS system with a similar priority based hierarchy control.

The new task set, defined in figure 11, enhances the dexterity and human-robot interaction of the teleoperated platform. The main task, with the highest priority, is the control of the tool tip of the fetoscope, teleoperated from the master station or with manual guidance using co-manipulation. The three additional control strategies desired are defined as secondary tasks that will be performed in the null-space. Figure 12 shows the proposed control architecture with priority-based hierarchy.

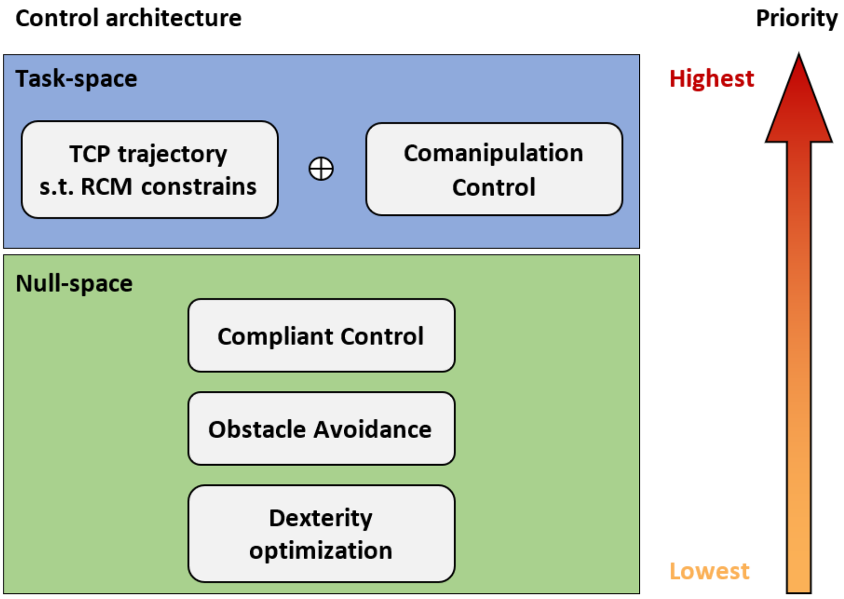
Control architecture
Priority
Task-space
TCP trajectory s.t. RCM constrains
⊕
Comanipulation Control
Null-space
Compliant Control
Obstacle Avoidance
Dexterity optimization
Highest
Lowest

Figure 12: Proposed control architecture with priority-based hierarchy using the null-space projection. Subtasks are designed to improve the dexterity and human-robot interaction of the teleoperated system.

The multi-task approach treat the new features of the system as modules with a priority level. These modules can be enabled or disabled from the main surgeon command station. During the surgery phase the control mode, which includes the TCP trajectory as main task, can have the three subtasks enabled simultaneously, or a combination of them. In the pre-operatory setup and the post-operatory removal of the tool, the control mode has the co-manipulation control as main task, which allows the surgeon to manually the end-effector of the robot. In this phase, the subtasks of dexterity optimization and compliance control can provide the optimal configuration of the robot with respect to the commanded end effector pose.

3 Optimization of dexterity exploiting redundancy in RMIS

In RMIS, the robot kinematics are strongly constrained by the Remote Center of Motion, defined by the fulcrum point. Consequently, the manipulator dexterity, which indicates the motion performance in the task space, is severely affected. The trocar insertion defines a RCM over which the tool pivots. This imposes the tool to pass through the trocar to access to the surgical workspace. The RCM also inverts the motion paradigm, a forward movement of the tool tip is executed with a backward movement of the end effector. Other constrains come from the need of continuity in joint values, which is achieved by limiting the robot possible inverse kinematics (IK) solutions to left handed, elbow up and wrist no-flip. This limitation avoids sudden changes in the configuration, which would cause an abrupt increase in speed and cause damage to the patient. Moreover, the robot often reaches joint limits or singularities due to the constrained workspace, which decreases the dexterity. In order to increase the dexterity of the robot in a constrained workspace, this work exploits the benefits of redundancy in the kinematic problem.

Kinematic redundancy occurs when a robotic manipulator has more degrees of freedom than those required for a given task. A general spatial task requires 6 DoF, three for position and three for orientation, therefore a 7 DoF robot become redundant for this task. For a given position and orientation of the end effector, the redundant robot has infinite possible configurations. Since dexterity is directly related to the joint configuration of the robot, it can be optimized choosing the best option from the infinite solutions of the redundant manipulator.

The KUKA Lightweight robot is an anthropomorphic manipulator with 7 DoF. The extra joint is a revolute actuator located in the third position of the joint configuration, between the robot's "shoulder" and the "elbow". Figure 13 shows a schematic representation of the robot. This extra joint is referred as the external joint in the KUKA documentation. The redundancy of the KUKA LWR can be used to generate infinite arm configurations without changing the wrist pose.

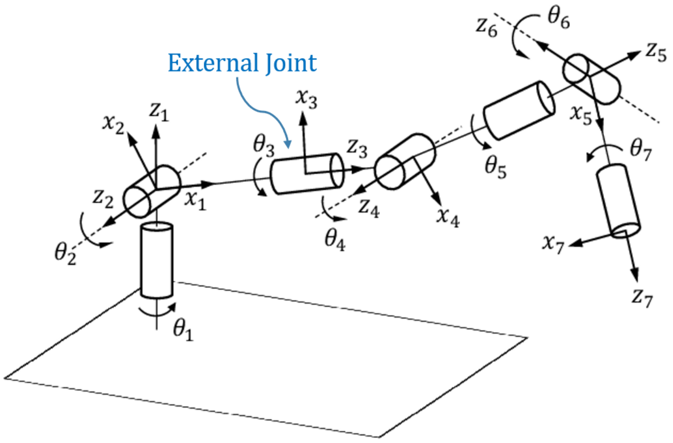

Figure 13: Schematic representation of KUKA Lightweight robot. The external joint is labeled as θ_3.

Research in kinematic redundancy has been active for more than two decades. Redundancy has been already studied for dexterity parameters maximization [31]-[32], for obstacle avoidance [33]-[34] and for collision management [35]. Other uses of redundancy are reduction of impact force [36] and fault tolerance [37]. The contribution of this work lies on the exploitation of redundancy to increase the surgical teleoperation system performance.

3.1 Dexterity of a robotic manipulator

Kinematic dexterity is a measure of the capability of the robot to execute a specific task in a given configuration. Dexterity can be analyzed through several parameters which depend on the manipulator configuration. Considering a robotic manipulator with n DoF for a task in m dimensional space, where $m \geq n$, the position of the end effector is obtained through the robot's forward kinematics

$$X = f(q) \tag{3.1}$$

Where $q = [q_1 \; \cdots \; q_n]^T \in \mathbb{R}^n$ and $X \in \mathbb{R}^m$. The derivative of 3.1 gives the differential kinematics equation (3.2).

$$\dot{X} = J(q)\dot{q} \tag{3.2}$$

The manipulator Jacobian matrix (J), in the form of a $m \times n$ matrix, represents the relation between the joint velocities and the linear and angular velocities of the end effector.

One of the most used dexterity index is manipulability. Manipulability represents the capacity of a robot to generate a movement from a given configuration. A higher manipulability value indicates that the robot has more capacity of movement. This index is computed with the Jacobian and is defined as

$$w(q) = \left| det(J(q)) \right| \tag{3.3}$$

The Jacobian of a redundant robot has more columns than rows $(n > m)$ which makes the Jacobian non-square. Since the determinant of a non-square matrix cannot exist, the manipulability for a redundant robot is defined as

$$w(q) = \sqrt{det(J(q)J^T(q))} \tag{3.4}$$

The manipulabilty index $w \in \mathbb{R}^+$ since the product JJ^T is positive semi-definite. A manipulator in a singular configuration has $w = 0$ because it has one or more eigenvalues of JJ^T equal to zero. Singularities occur inside the workspace and are caused by the alignment of two or more joint axes, causing the loss of DoF. When a robot falls into a singularity or moves in its surroundings, performs large motions in joint space for small movements in Cartesian space, which causes undesirable motions.

The singular values (σ_m) of the Jacobian matrix can be obtained from the Singular Value Decomposition (SVD) method (3.5). The singular values represent the manipulability in the direction of each axis. The minimum singular value (MSV) indicates the worst case scenario. Manipulability can be represented as an ellipsoid where the eigenvectors of JJ^T define the principal axes and the singular values the length.

$$J = U\Sigma V^T \implies \Sigma = \begin{bmatrix} \sigma_1 & 0 & \cdots & 0 \\ 0 & \sigma_2 & \cdots & 0 \\ \vdots & \vdots & \ddots & \vdots \\ 0 & 0 & \cdots & \sigma_m \end{bmatrix} \tag{3.5}$$

The ratio of the maximum singular value (σ_{max}) to the minimum singular value (σ_{min}) is called condition number (3.6) and is used as another dexterity index. Condition number (CN) indicates the anisotropy of the motion and denotes the ill-conditioning of J. A $CN = 1$ indicates a spherical shaped manipulability ellipsoid. Consequently, the robot presents the same movement capacity in all directions.

$$CN(q) = \frac{\sigma_{max}}{\sigma_{min}} \tag{3.6}$$

On the contrary, isotropy (Δ) is the dexterity index used to represent the uniformity of motion ability in all directions from a given pose. Isotropy is calculated as the ratio between the geometric mean of the Jacobian matrix and the arithmetic mean of its eigenvalues (3.7). The arithmetic mean of the eigenvalues is obtained through the trace of the matrix JJ^T.

$$\Delta = \frac{(det(JJ^T))^{1/m}}{trace(JJ^T)/m} \tag{3.7}$$

where $\Delta \in (0, 1)$. A value of $\Delta = 1$ indicates optimal dexterity and $\Delta = 0$ indicates a singularity.

Detecting the proximity to a singularity is crucial for a safe motion inside the surgical workspace. Upon the dexterity indices described above, manipulability and isotropy are valid options for the requirements of this work. Both can be used to prevent the robot from falling into a singularity. Maximizing these dexterity indices by means of the redundant joint will decrease the risk of entering in a singularity in ill-positioned workspaces.

3.2 Analysis of kinematic redundancy benefits on dexterity in RMIS

As explained above, dexterity depends on the configuration of the robot for a determined pose. As redundancy gives multiple solutions to the IK problem, dexterity will vary depending on the configuration given by the external joint (q_3) value. The parametrization of the variation in dexterity by means of redundancy is a key factor to assess the value of a redundant manipulator in RMIS. In order to quantitatively analyze the effects of redundancy on dexterity, a simulation of a redundant robot performance in a RMIS workspace has been conducted.

A Matlab simulation environment is prepared with a KUKA LBR iiwa equipped with a fetoscope, as well as a trocar insertion, to simulate the robot-assisted FMIS. This simulation environment is explained in the section 1.6. The workspace of the robot is constrained with the RCM, which defines a cone-shape workspace. The workspace is sampled to obtain a homogeneous distribution of points inside it. The sampling is performed with the division of the cone in various XY planes along the Z axis. In each XY plane of the workspace, a homogeneous distribution of points based on polar coordinates is scattered (fig. 14).

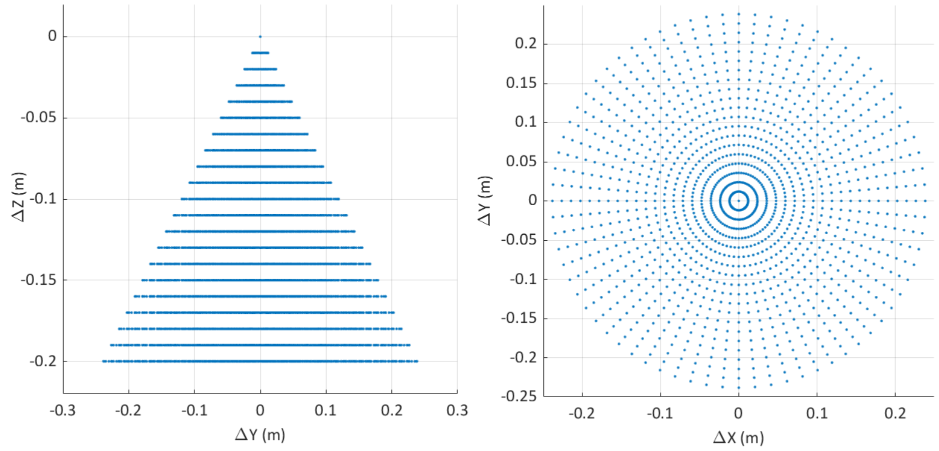

Figure 14: Sampled FMIS workspace. Left: side view shows the division in Z axis. Right: top view shows the distribution in polar coordinates.

Inside this simulation environment, the tip of the fetoscope is moved along the workspace and, at each point, several configurations are computed forcing different q_3 values (fig. 15). The configurations are computed through the inverse kinematics of the robot. The inverse kinematic problem is constrained to the configurations left handed, elbow up and wrist no flip. Additionally, the end effector cannot go below the trocar height to avoid colliding with the patient. The orientation of the end effector is also constrained by the trocar, therefore the fetoscope is always passing through the RCM. As the external joint value is fixed previously, the redundancy does not affect the inverse kinematic resolution in terms of computational complexity.

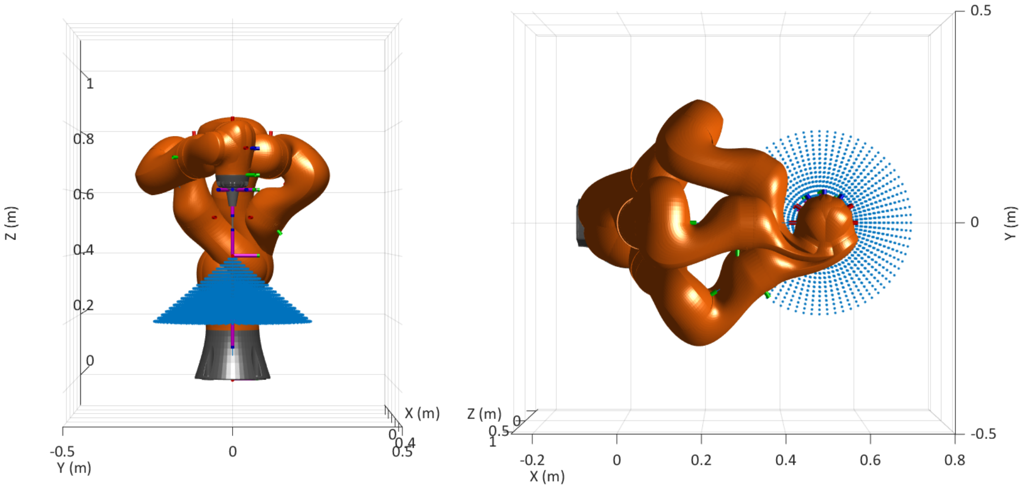

Figure 15: Example of various configurations with the same end effector pose for $q_3 = -\pi$, $q_3 = 0°$ and $q_3 = \pi$.

The dexterity indices of manipulability, MSV, CN and isotropy are calculated at all the points of the workspace, for each redundant configuration. With this method, a dexterity dataset of redundant configurations for the whole workspace is obtained. The outcomes of the analysis of the dataset obtained with this experiment are presented below.

The first issue addressed from the results of the experiment is the effect of redundancy in the robot's workspace. The reachability workspace represents the capacity of the robot to reach a position in the operational space. The dexterity workspace represents the capacity of the robot to reach a position in the operational space in any orientation. The used IK solver indicates whether it has been possible to obtain a result within the imposed limitations. The evaluation of this parameter can give an idea of the robot's available workspace. During the experiments it has been detected that the IK solver algorithm returns some solutions as not reached, despite being a correct configuration that fulfills the kinematic restrictions. To avoid false negatives in the reached parameter, the kinematic configurations obtained from the inverse kinematics solver are double checked using the forward kinematics (FK) of the robot. Therefore, the algorithm described hereafter (Alg. 1) calculates the distance error between the desired and the computed position of the fetoscope tip (TCP) and the deviation of the fetoscope from the trocar point. Both errors are checked to see if they are within tolerances and the parameter reached is corrected accordingly.

Algorithm 1: Validity check of IK solutions

```
Input: Desired TCP position $P$, trocar position $P_{tr}$, IK solution configuration $q$ and error
       tolerances $Tol_{dist}$ and $Tol_{aim}$
Result: Check if the fetoscope is at the desired position and passes through the trocar
$P_{ee} = FK(q, endeffector)$              // Get the position of the robot end effector

$P_{tcp} = FK(q, TCP)$                     // Get the position of the fetoscope tip (TCP)

$Error_{dist} = \|P - P_{tcp}\|_2$         // Distance error from the desired point

$\vec{v_1} = P_{tcp} - P_{ee}$             // Vector from end effector to fetoscope tip

$\vec{v_2} = P_{tr} - P_{ee}$              // Vector from end effector to trocar

$Error_{aim} = \|\vec{v_1} \times \vec{v_2}\|_2$   // If $\vec{v_1} \parallel \vec{v_2} \implies \vec{v_1} \times \vec{v_2} = 0$

if $Error_{dist} \leq Tol_{dist}$ & $Error_{aim} \leq Tol_{aim}$ then
    $isValid(q) = true$
else
    $isValid(q) = false$
end
```

The variations in the robot's workspace caused by redundancy can be measured from two performance indices: the number of reached points inside the surgical workspace and the volume of the reachable workspace. To evaluate the differences provided by the redundant configurations to the reachability of the robot, the number of reached positions inside the surgical workspace are computed for several redundant configurations of the manipulator. In FLP surgery, the trocar position and orientation depends on the position of the placenta, which can be in anterior, posterior, fundal or lateral position. To deal with such different scenarios, two surgical workspaces with different orientations have been tested. The first workspace (fig. 16a) simulates the most common placenta orientation, which is a posterior placenta, and is well positioned respect to the robot. The second workspace (fig. 16b), which simulates a lateral placenta, has a cumbersome orientation.

Forcing $q_3 = 0$, the LWR losses a DoF and becomes a non-redundant manipulator. The variation in the reachability obtained by redundancy is defined as the ratio

$$\Delta Reachability(\%) = \frac{\sum newPoints}{\sum WS_{NRM}} \times 100 \tag{3.8}$$

where WS_{NRM} is the set of points reached by the manipulator with non-redundant configurations ($q_3 = 0$) and $newPoints$ is a set of points such that

$$newPoints \in WS_{RM} \mid newPoints \notin WS_{NRM} \tag{3.9}$$

where WS_{RM} is the set of points reached by the manipulator with any redundant configuration ($q_3 \in (-\pi/2, \pi/2)$).

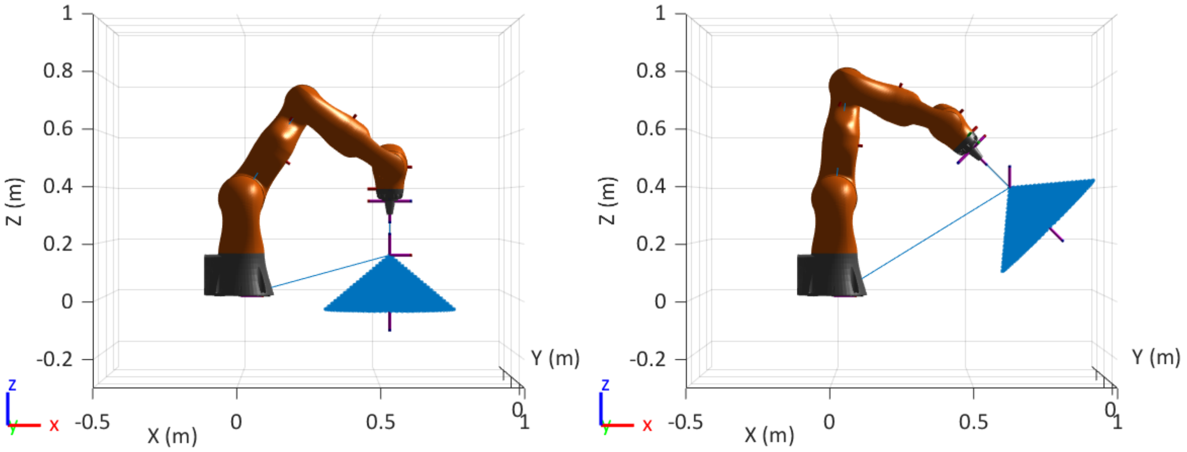

(a) (b)

Figure 16: Different workspaces defined by the orientation of the trocar. (a) well-positioned workspace (b) ill-positioned workspace.

The volume of the workspace can be approximated by the volume of its convex hull. The convex hull of a set X of points in the Euclidean space is the smallest convex set that contains X. The variation of the workspace volume due to redundancy can be calculated as

$$\Delta V_{WS}(\%) \approx \frac{V_{CH_{RM}} - V_{CH_{NRM}}}{V_{CH_{NRM}}} \times 100 \tag{3.10}$$

where CH_{RM} is the convex hull of the redundant manipulator's workspace and CH_{NRM} is the convex hull of the non-redundant manipulator's workspace.

Figure 17 shows the results of the workspace analysis. The results prove that in a well-positioned workspace, the reachability increases a 30% but there is not a significant volume increase. In the ill-positioned workspace, the reachability increases up to a 80% and the external volume of the workspace up to a 70%. This significant increase in the ill-conditioned workspace is due to the fact that, in such orientations, a non-redundant robot is prone to fall into singularities whereas a redundant robot can avoid them exploiting kinematic redundancy.

The second aspect addressed from the results of the experiment is the effect of redundancy on dexterity. The increase of dexterity obtained using redundant with respect non-redundant

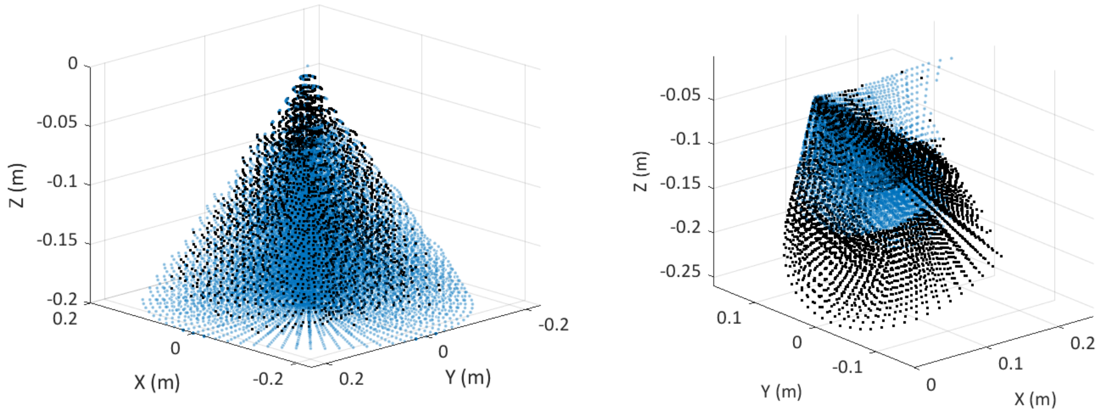

(a) (b)

Figure 17: Reachability increment in workspace due to redundancy. Blue points represent positions in workspace reached by a non-redundant robot. Black points represent positions only reached with a redundant robot.

configurations to assert the benefits of redundancy is analysed using the same dataset. Non-redundant configurations have been obtained by fixing $q_3 = 0$, obtaining the typical configuration of a 6 DoF serial robot. Figure 18a shows the manipulability values of the non-redundant manipulator configurations for a given XY plane of its workspace. This manipulability values are used as baseline values in the comparison between non-redundant and redundant robot's performance. Figure 18b shows the maximum ratio between the manipulability value of any redundant configuration, given by $q_3 \in (-\pi/2, \pi/2)$, and the corresponding baseline value.

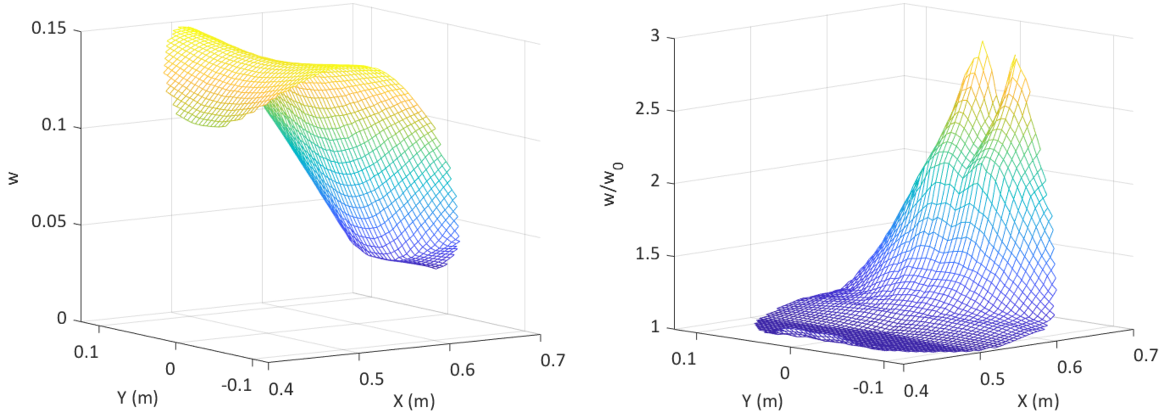

(a) (b)

Figure 18: Manipulability value in the workspace. Robot base at $P_B = [0, 0, 0]$. (a) Manipulability value for non-redundant configurations (baseline values). (b) Maximum ratio between manipulability of redundant configurations and baseline values.

The manipulability of the non-redundant robot shows that, in some regions of the workspace, the further points with respect to the robot's base, lead the robot toward a singularity ($w \approx 0$). This is consequence of the alignment of two or more axis of the robot, caused by the kinematic restriction of the RCM. The maximum ratio shows that manipulability can be increased up to three times in areas close to a singularity, as using the redundant joint can avoid the alignment of the robot's axis.

Concerning CN dexterity index, figure 19a shows the obtained results using the $XY = 0$ plane (same as used in figure 18) for a non redundant manipulator ($q_3 = 0$). Again, this CN values are used as baseline values in the comparison between non-redundant and redundant performance. A higher CN value represents a more anisotropical motion in the Cartesian Space, consequently in this case the objective is minimizing the CN by means of redundancy. Figure 19b shows the minimum ratio between the CN value of any redundant configuration, given by $q_3 \in (-\pi/2, \pi/2)$, and the corresponding baseline value.

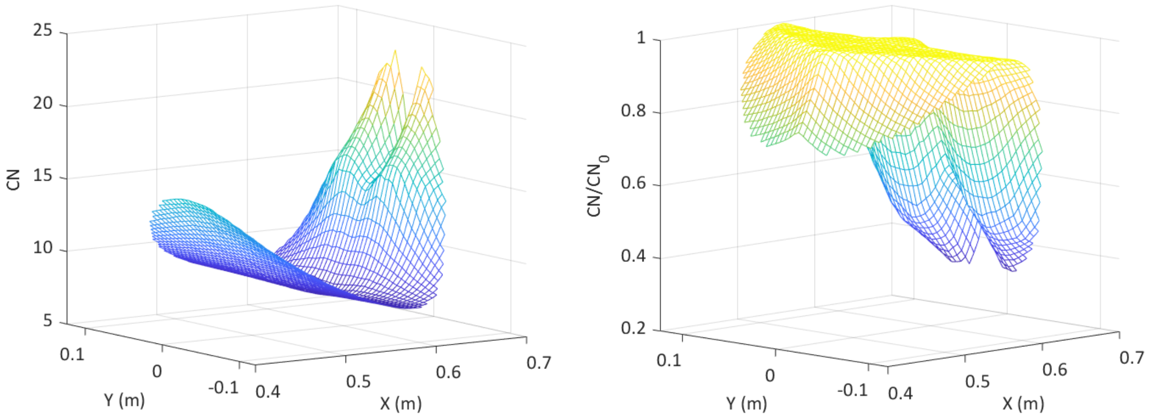

(a) (b)

Figure 19: Condition Number value in the workspace. Robot base at $P_B = [0, 0, 0]$. (a) CN value for non-redundant configurations (baseline values). (b) Minimum ratio between CN of redundant configurations and baseline values.

The CN of the non-redundant manipulator configurations shows that in the further points with respect to the robot's base of the workspace, the robot's motion performance in the different Cartesian axis is highly different. The minimum ratio shows that the CN can be decreased up to one-third of the baseline value in some areas.

The isotropy index, contrary to the CN, represents the homogeneity of the motion performance in the Cartesian Space, where the optimum isotropy is represented by the maximum value of the index. Figure 20a shows the isotropy values of the non-redundant manipulator ($q_3 = 0$), for the same XY plane of its workspace as before. In this case, the objective is, again, maximizing the index value. Figure 20b shows the maximum ratio between the isotropy value of any redundant configuration, given by $q_3 \in (-\pi/2, \pi/2)$, and the correspondent baseline value.

The isotropy index of the non-redundant manipulator shows that the value decreases in the same region of poor performance obtained by the previous indices (see figures 18a and 19a). The maximum ratio shows that the isotropy can be increased up to a 50% in the problematic areas.

As expected, the results of the dexterity analysis prove that the use of a redundant manipulator increases the dexterity performance. The major increment is obtained in situations where a non-redundant manipulator presents poor performance, mostly in the vicinity of a singularity. As seen in the dexterity indices ratios between redundant and non-redundant configurations, in the worst case the redundant manipulator has the same performance as the non-redundant manipulator. This derives from the fact that redundancy contains, as one of the solutions to the IK problem, the same configuration as the non-redundant.

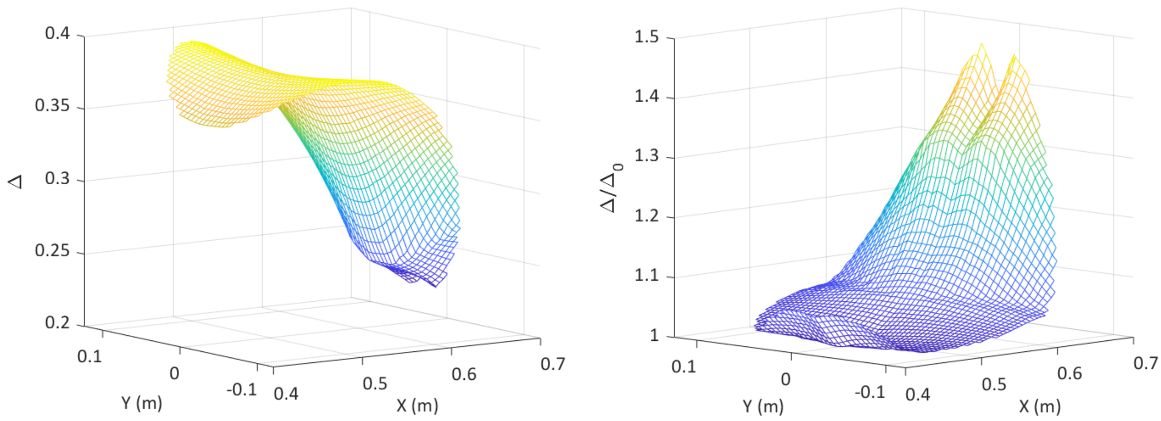

(a) (b)

Figure 20: Isotropy value in the workspace. Robot base at $P_B = [0, 0, 0]$. (a) Isotropy index for non-redundant configuration. (b) Maximum isotropy ratio between redundant and non-redundant configurations.

Therefore, having proved both the increment in dexterity and in reachability in a RMIS environment, it has been demonstrated that exploitation of a redundant robot in the HATTTS teleoperated platform can increase the surgical task performance.

3.3 Dynamic manipulability optimization in RMIS

The analysis conducted in the previous section proves that the dexterity of the robot in the RMIS workspace can be optimized exploiting redundant configurations. The use of a redundant robot in a teleoperated platform, such as the KUKA LWR, opens the possibility to a dynamic optimization of dexterity. The manipulability index is chosen to optimize dexterity, as it requires less calculation and is therefore more computationally efficient. In addition to manipulability, the isotropy value is still computed in the experimental phase to ensure that homogeneity in the motion performance is not compromised.

Following the multi-task approach proposed in section 2, a secondary task, performed in the null space, is responsible for the dexterity enhancement. This subtask maximizes dexterity through dynamic optimization of manipulability exploiting redundancy in incremental motion (DOMERIM). The proposed algorithm, described in Alg. 2, maximizes the manipulability of the redundant robot in each step of its trajectory in the Cartesian space. For each new point of the trajectory, a fixed number of configurations are calculated by setting the value of the redundant joint near the previous q_3 value. This approach ensures local optimization. The global optimization is not realistic because it demands infinite joint accelerations to reach optimal joint configuration. A more realistic approach has been used, restricting the incremental joint movements in terms of displacement and velocity. The local optimization criteria ensures smooth motions, which are a priority in the surgical task as they provide greater safety. The chosen q_3 values must be within boundaries set by a predefined policy. This policy can change the boundaries in function of the distance of the TCP from the RCM. From the candidate configurations, the one with maximum manipulability is chosen.

To test the manipulability optimization algorithm, a randomized path is generated inside the surgical workspace. This path (fig. 21) includes movements along the edge of the workspace,

Algorithm 2: Dynamic Optimization of Manipulability Exploiting Redundancy in Incremental Motion (DOMERIM)

```
Input: Next trajectory point $P(t)$ and previous configuration $q^*(t-1)$
Output: Next configuration $q^*(t)$ with optimized manipulability
initialization
foreach new $P(t)$ do
    $p = P(t)$
    $q3NewValues = \begin{cases} q_3^*(t-1) - \Delta\theta \\ q_3^*(t-1) \\ q_3^*(t-1) + \Delta\theta \end{cases}$

    $q3Candiadates = \{\theta \in q3NewValues \mid \theta_{LBound} \leq \theta \leq \theta_{UBound}\}$

    foreach $\theta \in q3Candidates$ do
        $q = IK(p) \rightarrow$ s.t. $q_3 = \theta$
        $qData(\theta) = \begin{bmatrix} q & w(q) & CN(q) & \Delta(q) \end{bmatrix}$
    end
    $q^* = \{q \in qData \mid w(q^*) = max(w(q))\}$
end
```

which, added to the kinematic constrains of the RCM, forces the robot to reach singularities. The sampling time used is $T = 0.01s$ and the duration of the test is $t = 10s$.

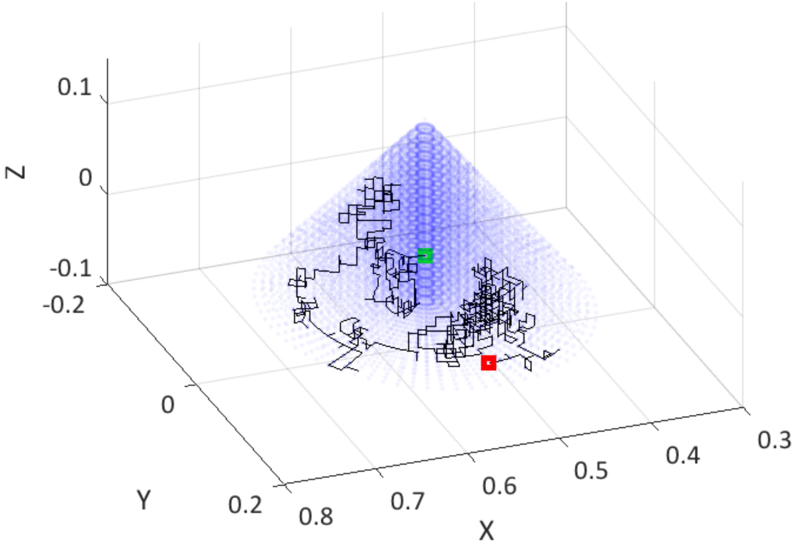

Figure 21: Path defined for the dynamic optimization test. Initial position in green and final point in red.

The first test for the optimization algorithm is performed with a fixed boundary policy to study the behaviour of the robot when the DOMERIM algorithm is applied. This policy sets the boundaries to $(-\pi/2 \leq q_3^* \leq \pi/2)$ for all the workspace (fig. 22a), allowing the robot to move to an optimal configuration without any constrain. Figure 22b shows the resultant optimal q_3^* value (in blue) that allow the maximum manipulability configuration, through all the robot's trajectory, and the baseline q_3 value (in red). Figure 22c shows the manipulability value, normalized with the baseline manipulability value (w_0), for all the computed optimum joint configurations in the manipulator's path. Figure 22d shows the isotropy value, normalized with the baseline isotropy value (Δ_0), for all the computed optimum joint configurations in the manipulator's path.

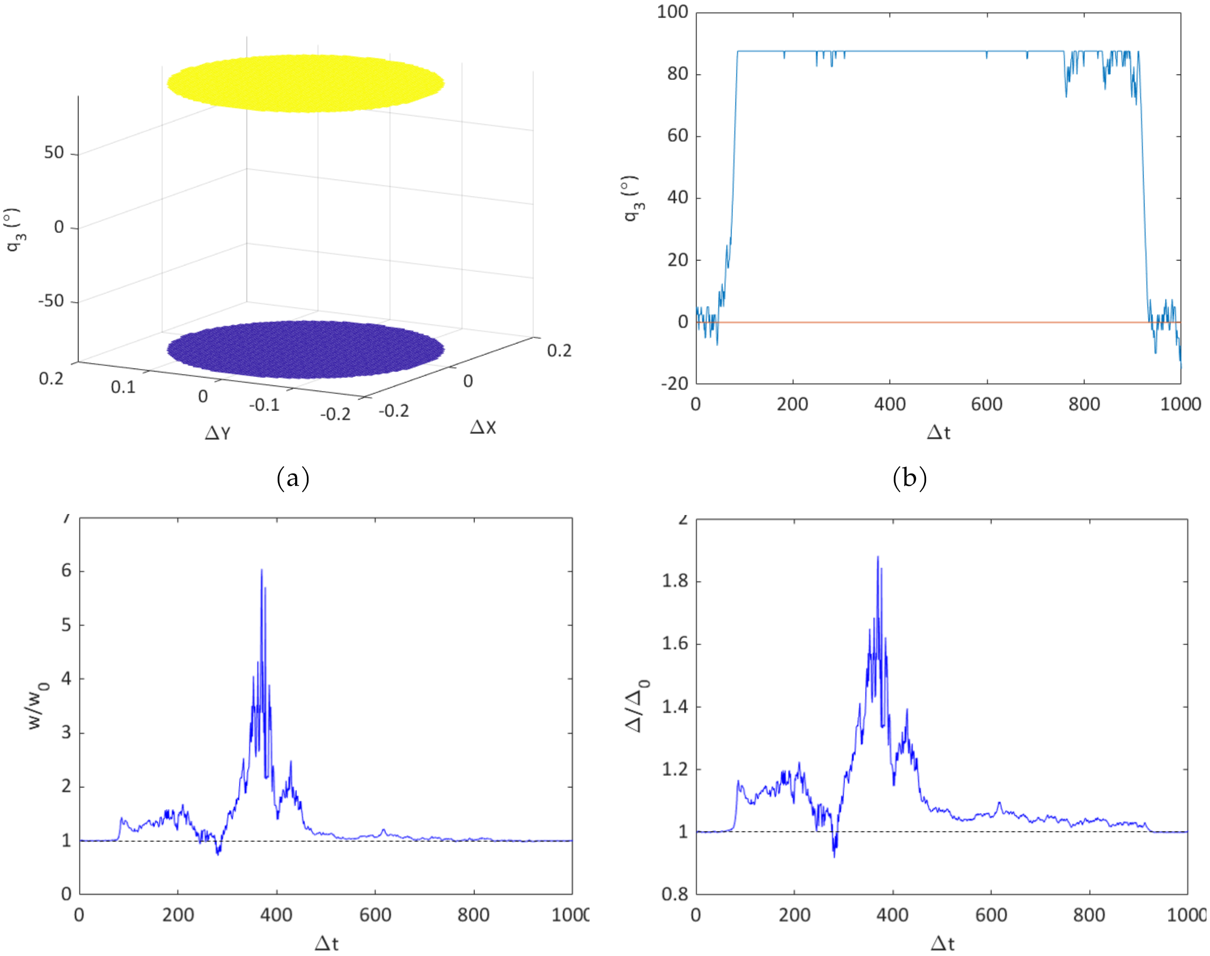

(a) (b)

(c) (d)

Figure 22: Dynamic optimization with fixed boundaries policy. a) q_3 upper bound, yellow, and q_3 lower bound, in blue. b) q_3^*, in blue, and q_{3_0}, in red. c) Optimized configuration's manipulability normalized with w_0. d) Optimized configuration's isotropy normalized with Δ_0.

The results of DOMERIM show an increment of manipulability up to seven times compared to the baseline value. Moreover, isotropy has also increased (reaching a maximum of 80% improvement). In this case, the robot remains almost all the trajectory with $q_3^* = \pi/2$ as it has the maximum value of manipulability. However, as seen in figure 22c and 22d, there are some robot configurations where both manipulability and isotropy fall below 1. In that moment, the computed optimal configuration manipulability is lower than the non-redundant configuration. The robot remains in configurations with the same q_3^* value (maximum manipulability of its neighbourhood) but exists the possibility of not being a global maximum. Hence, the fixed boundary policy can lead the robot to fall in a manipulability local maximum. Nevertheless, if the gradient between the q_3 optimal value of two consecutive points of the workspace is higher than the allowed increment of the q_3, reaching the optimal value requires several control steps.

Two main aspects influence in local maximum reachment: first, the location of the robot basis with respect the RCM and the workspace. Second, the trajectory followed when a local maximum is reached. After reviewing these two aspects in the experiments, the conclusion is that in some points of the workspace where $Y = 0$, the q_3 value that gives the maximum manipulability has an asymptotic behaviour. On the left side of the workspace from the robot's base frame of reference ($Y = 0^+$), the maximum manipulability could be reached with $q_3 = -\pi/2$ while on the right side ($Y = 0^-$), the maximum manipulability could be reached with $q_3 = \pi/2$. In the surroundings of these points, both $q_3 = -\pi/2$ and $q_3 = \pi/2$ are local maximums. The gradient between two consecutive points that crosses zero in that region is significantly higher than the allowed q_3 step increment, which prevents the robot from escaping the local maximum.

To overcome this issue, a new boundary policy is proposed, setting the upper and lower boundary proportional to the linear distance in the Y axis. Therefore the robot is forced to have $q_3 = 0$ when $Y = 0$, ensuring a proper transition from side to side. Figure 23 shows the results obtained with the dynamic optimization algorithm following this new policy.

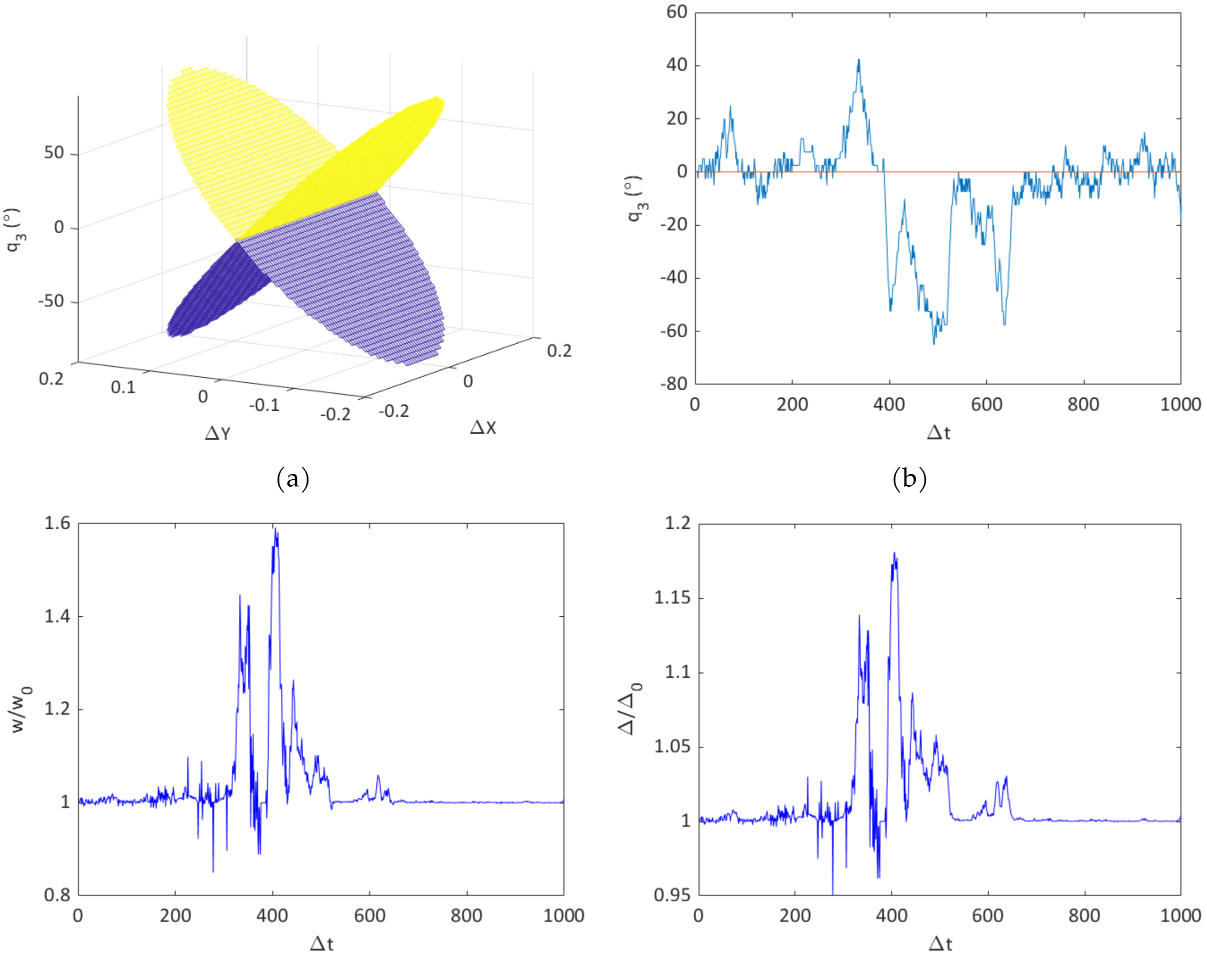

(a)

(b)

(c)

(d)

Figure 23: Dynamic optimization with linear boundaries policy. a) q_3 upper bound, yellow, and q_3 lower bound, in blue. b) q_3^*, in blue, and q_{3_0}, in red. c) Optimized configuration's manipulability normalized with w_0. d) Optimized configuration's isotropy normalized with Δ_0.

Figure 23a shows the bound values in the linear boundary policy. Figure 23b shows the resultant optimal q_3^* value (in blue) that permits the maximum manipulability configuration, through all the robot's trajectory, and the baseline q_3 value (in red). Figure 23c shows the manipulability value, normalized with the baseline manipulability value (w_0), for all the computed optimum joint configurations in the manipulator's path. Figure 23d shows the isotropy value, normalized with the baseline isotropy value (Δ_0), for all the computed optimum joint configurations in the manipulator's path.

The results of the dynamic optimization algorithm, despite having an increase in manipulability of up to 60% with respect to non-redundant configurations, show a lower overall manipulability than with the previous policy. The computed optimal q_3^* crosses zero several times which entails a higher motion range. Despite the fact that manipulability is not increased as much as with the fixed boundaries policy, this policy makes the robot remain in a more vertical configuration. Vertical configurations make the robot occupy less volume of the shared workspace, freeing up space for the auxiliary medical staff. Furthermore, this policy allows the robot to have greater capacity to modify its configuration since it uses the central range of q3 configurations. If it is lateralized, in spite of having greater manipulability, it loses reconfiguration options as it is limited on one side.

With the objective of defining a strategy that combines the advantages and minimizes the disadvantages of the two previous, a new boundary policy is defined. This new boundary policy sets the upper and lower boundary proportional to the radial distance to the RCM in the XY plane (fig. 24a). With radial boundaries, the robot can achieve the maximum manipulability in positions where could not be reached with the linear policy. On the other hand, it forces the robot to decrease its q_3 value near the center. Therefore if the robot is in a local maximum, it can escape when the robot trajectory moves along the center.

The DOMERIM algorithm is tested again with the same path and the new boundary policy. Figure 24b shows the resultant optimal q_3^* value (in blue) that forces the maximum manipulability configuration, through all the robot's trajectory, and the baseline q_3 value (in red). Figure 24c shows the manipulability value, normalized with the baseline manipulability value (w_0), for all the computed optimum joint configurations in the manipulator's path. Figure 24d shows the isotropy value, normalized with the baseline isotropy value (Δ_0), for all the computed optimum joint configurations in the manipulator's path. The results prove that this proposed policy combines the advantages of both previous policies. The manipulability value for the computed optimal configurations increases up to seven times compared with w_0. Additionally, the manipulability does not decrease with respect to w_0, which means that the robot can escape from local maximums. This is confirmed with the values of q_3^*, that show a change between positive and negative joint angles.

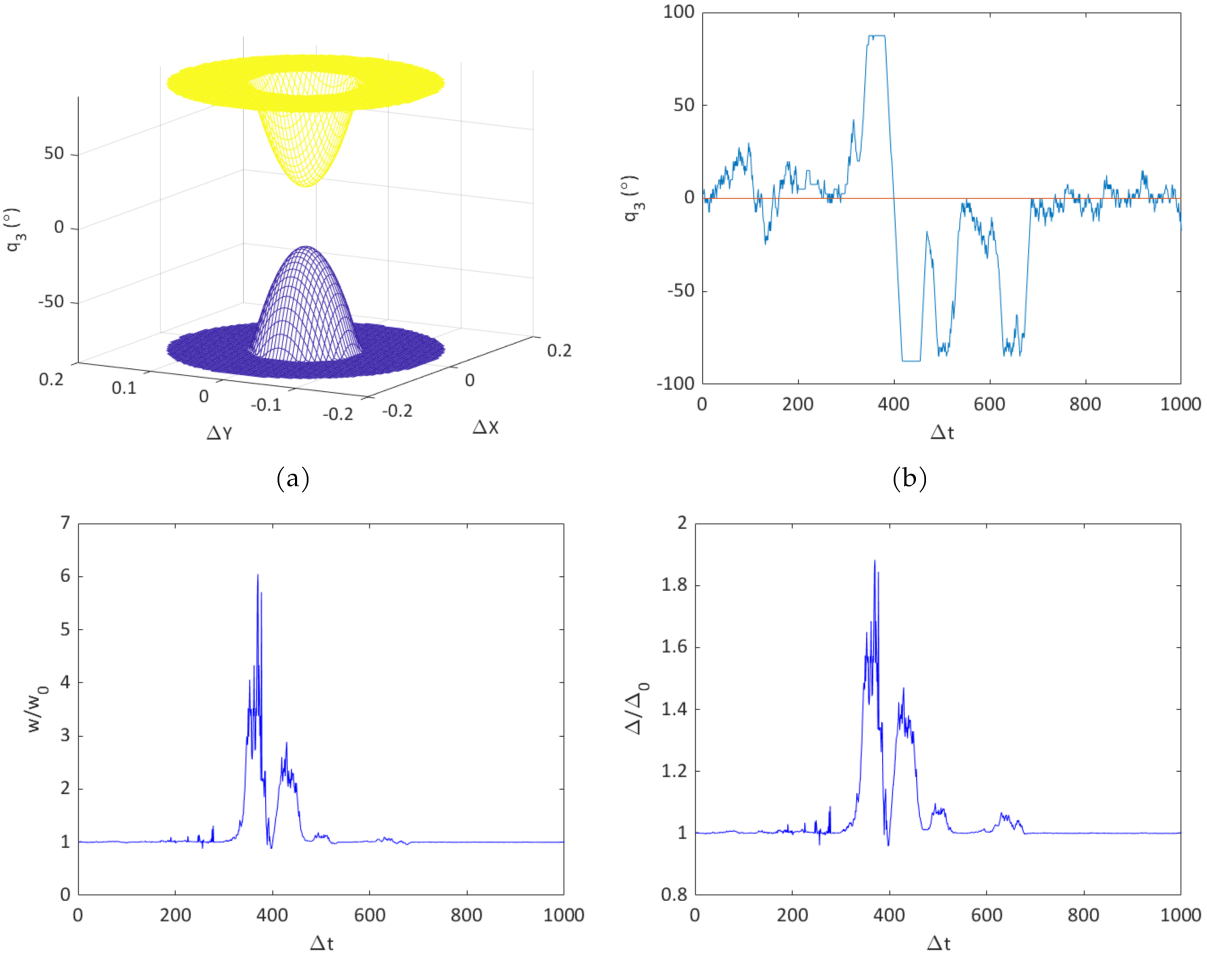

(a) (b)

(c) (d)

Figure 24: Dynamic optimization with radial boundaries policy. a) q_3 upper bound, yellow, and q_3 lower bound, in blue. b) q_3^*, in blue, and q_{3_0}, in red. c) Optimized configuration's manipulability normalized with w_0. d) Optimized configuration's isotropy normalized with Δ_0.

Figure 25 represents a small sample of the DOMERIM algorithm applied to an RMIS task. Figure 25a shows the initial configuration of the robot. Figures 25b to 25i represent consecutive steps of the computed optimal configuration (highlighted) and the non-redundant configuration (ghost) for the same given position.

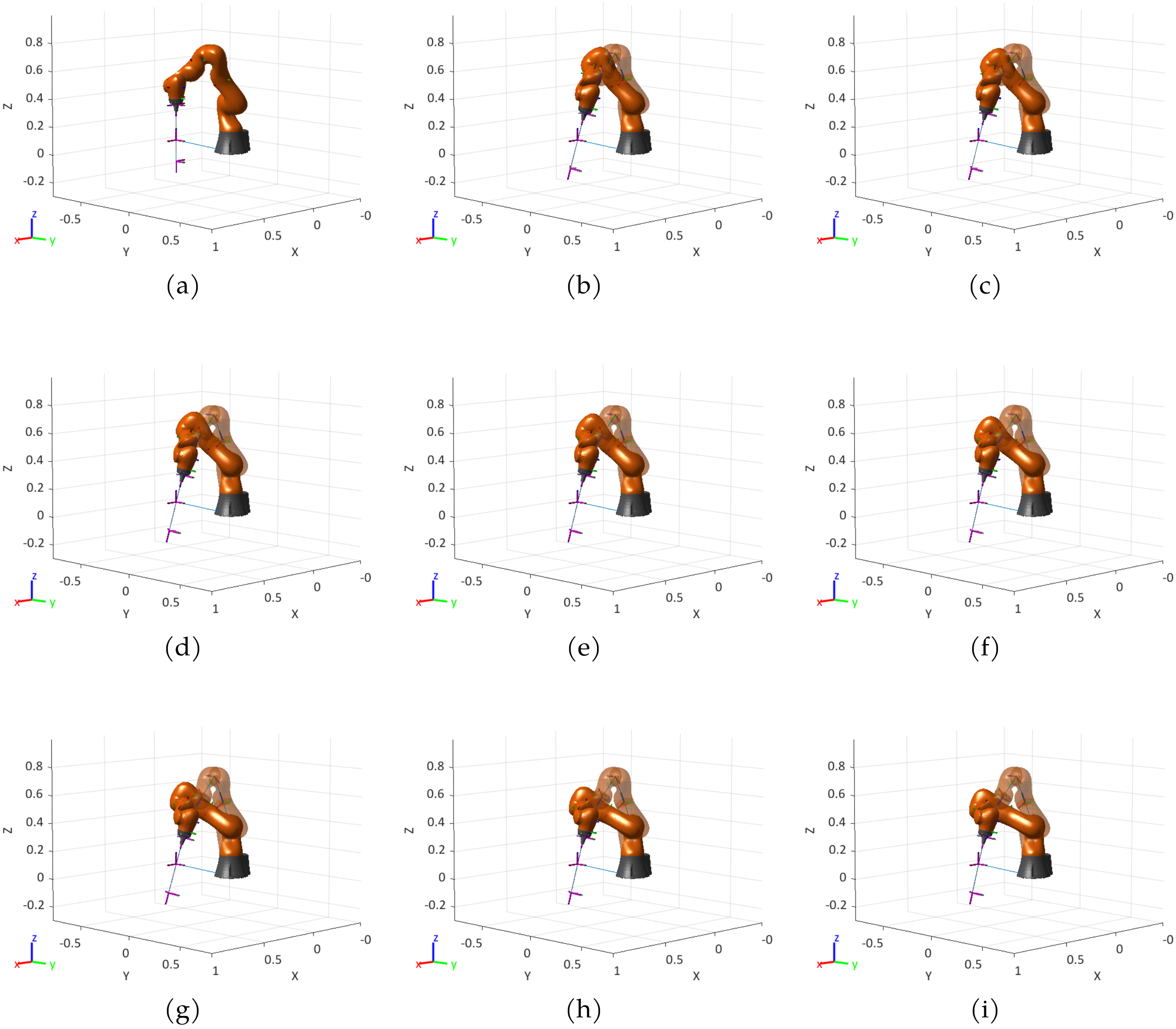
0.8
0.6
0.4
0.2
0
-0.2
Z
-0.5
0
0.5
1
Y
0.5
0
-0
X
z
x
y

(a) (b) (c)

(d) (e) (f)

(g) (h) (i)

Figure 25: Example of optimized configuration with DOMERIM (highlighted) vs non-redundant configuration (ghost). a) Initial configuration. b-i) Sequence of consecutive motions.

4 Human-robot interaction strategies for surgical robots

This chapter deals with the solutions provided by the human-robot control strategies within the field of RMIS. In order to focus the problem on FLP, the reality of the shared surgical space during surgery has to be understood. In the manual approach, the surgeon guides the fetoscopy with one hand and fixes the depth of the trocar with the other hand (right and left hand). Apart from the main surgeon, an assistant surgeon is responsible for guiding the fiber optics for coagulation inside the fetoscope. In addition, another assistant surgeon is responsible for guiding a ultrasound probe for medical imaging. There are usually more surgical staff within the workspace. This distribution means that the surgeon cannot work ergonomically and therefore accuracy and repeatability can be affected. The teleoperation approach improves this situation: the main surgeon uses a master station to guide the robot ergonomically and without interaction with other surgical staff. However, the other people needed during surgery continue sharing work space with each other and with the robot. This fact requires safety measures to avoid potential human-robot collisions while continuing with the execution of the surgery. Therefore, safe and controlled human-robot interactions (HRI) are critical in the surgical procedure. Collaborative strategies allow safe human-robot interactions, and permit the implementation of manual control of the robot by physical interaction.

Human-robot interaction inside the operating room has been a topic of research in the last years, with cornerstone works on co-manipulation [38], autonomous collaborative assistance [39] and safety[40]. The EU funded Smart Autonomous Robotic Assistant Surgeon (SARAS) project, with the participation of the GRINS research group, is working in the development of two autonomous auxiliary robots to free up the work space from medical personnel [41].

In this work, three HRI strategies are presented with different aims. The first strategy is an obstacle avoidance strategy, which changes the configuration of the robot arm to free occupied space when medical staff is approaching without physical interaction. This strategy does not require a collaborative robot, as it relies on an a external sensorial system that determines the position of the medical staff. The other two strategies are based on collaborative control, thus requiring a collaborative robot that senses external forces exerted over its body. A compliance control for collision reaction is proposed, allowing the surgeon to push the robot arm to free space when required while the position of the fetoscope tip is not altered. Finally, a co-manipulation control is discussed to allow a physical guidance of the robot to the trocar insertion in the pre-operative setup and post-operative removal (fetoscope extraction).

4.1 Obstacle avoidance strategy using robot redundancy

The usefulness of a redundant robot to maximize the dexterity of the manipulator has been proved in section 3.2. As seen in the experiments outcomes with the different boundary policies, the lateral occupancy of the redundant robot can be controlled. Therefore, the redundancy of the manipulator can be also used to optimize the occupancy of the shared human-robot surgical space. In several stages of the surgical procedure of FLP, the space surrounding the robot is used by an auxiliary surgeon, the sonographer or a nurse. Figure 26 shows a worst-case scenario, where the robot has two surgery assistants at both sides. This scenario entails a high collision risk.

Auxiliary medical staff can be considered as obstacles that must be avoided while the robot continues with the ongoing task. The perception of the obstacles and their position can be given

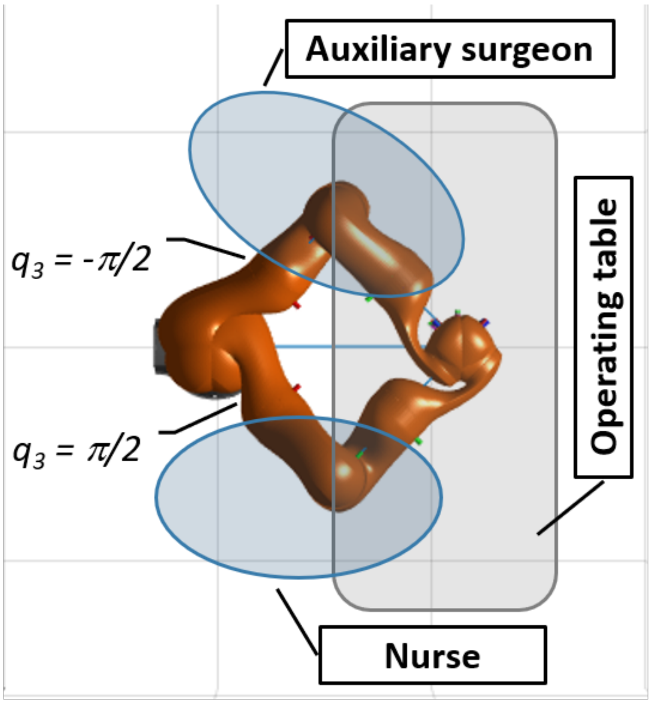

Figure 26: Representation of the space occupancy in the surgery room. Some of the redundant joint configurations enter the medical staff space.

by an external sensory system (e.g. vision system). An obstacle avoidance strategy exploiting redundancy can be used to create a safe shared space between medical staff and the redundant robot.

In the proposed strategy, the lateral space occupancy of the robot is restricted with lateral distance bounds. Lateral bounds define the upper and lower bound of the external joint (q_3) value. When an obstacle approaches the robot, pushes the lateral bound from the obstacle's side in the opposite direction. In consequence, the allowed occupancy space of the robot is reduced. In accordance to the multi-task hierarchical control proposed in section 2, this obstacle-avoidance strategy is defined as a secondary task with higher priority than the manipulability optimization task. Using this approximation, the optimization task maximizes the manipulability within the permitted bounds defined by the obstacle-avoidance strategy.

To develop a smooth and safe robot reaction in the obstacle avoidance policy, not only the distance of the obstacle is taken into account, but also the approximation velocity. Boundaries are defined as mass objects attached to an initial position via a mass-spring-damper node. The obstacle generates a repulsive potential field. This force field generates a repulsive force that pushes the boundary and free space for the obstacle (surgical staff). Figure 27 shows a schematic representation of the behaviour of a boundary limit when an obstacle approaches.

The initial position of the lateral bounds are obtained from the maximum and minimum lateral distance of the robot body in the redundant configurations at its initial position q_0 (4.1).

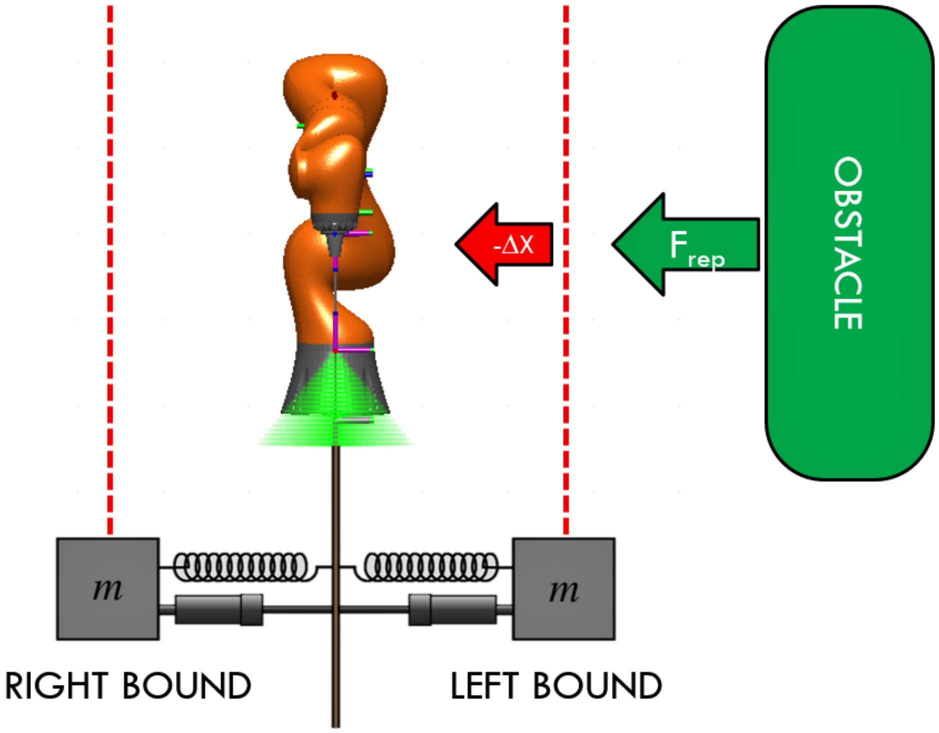

Figure 27: Representation of obstacle avoidance strategy exploiting redundancy and using potential repulsive fields and mass-spring-damped boundaries.

$$\left.\begin{aligned} Lbound_0 &= \underset{i}{max_y}(q_{0_i}) \\ Rbound_0 &= \underset{i}{min_y}(q_{0_i}) \end{aligned}\right\} \forall q_0 \mid q_{3_0} \in (-\pi/2, \pi/2) \tag{4.1}$$

When a force is applied to the body, the spring force is proportional to the displacement of the mass while the viscous damped force is proportional to the velocity. The dynamic state of the system is modelled by the equation

$$m\ddot{x}(t) + c\dot{x}(t) + kx(t) = f(t) \tag{4.2}$$

where m is the mass of the body, c the damping coefficient, k the spring constant and $f(t)$ the external force applied.

Being 4.2 a second order equation, its representation in the state space requires a reduction to first order equation. Therefore, position and velocity are chosen as the state variables (4.3).

$$\mathbf{x} = \begin{bmatrix} x_1(t) \\ x_2(t) \end{bmatrix} = \begin{bmatrix} x(t) \\ \dot{x}(t) \end{bmatrix} \tag{4.3}$$

The state space is represented with the first-order differential equations of x and the output equation as the position parameter. Therefore it becomes

$$\begin{aligned} \dot{\mathbf{x}} = \begin{bmatrix} \dot{x_1}(t) \\ \dot{x_2}(t) \end{bmatrix} &= \begin{bmatrix} 0 & 1 \\ -\frac{k}{m} & -\frac{c}{m} \end{bmatrix} \begin{bmatrix} x_1(t) \\ x_2(t) \end{bmatrix} + \begin{bmatrix} 0 \\ \frac{1}{m} \end{bmatrix} F(t) \\ y &= \begin{bmatrix} 1 & 0 \end{bmatrix} \begin{bmatrix} x_1(t) \\ x_2(t) \end{bmatrix} \end{aligned} \tag{4.4}$$

To ensure a stable behaviour of the mass-spring-dampers, the parameters k and c must make the matrix A stable (4.5). As the mass-spring-model parametrizes k and c as positive values, the eigenvalues of A will be always negative thus the matrix A will be stable (4.6).

$$A = \begin{bmatrix} 0 & 1 \\ -\frac{k}{m} & -\frac{c}{m} \end{bmatrix} \tag{4.5}$$

$$\lambda = eig(A) \implies Re[\lambda_i] < 0 \tag{4.6}$$

To solve the continuous-time differential equations in discrete-time, the implicit Euler method (4.7) is used to approximate the discrete state-space equations (4.8).

$$\dot{x}(k) \cong \frac{x(k+1) - x(k)}{T} \tag{4.7}$$

$$\begin{aligned} \begin{bmatrix} x_1(k+1) \\ x_2(k+1) \end{bmatrix} &= \begin{bmatrix} 1 & T \\ -\frac{kT}{m} & \frac{1-cT}{m} \end{bmatrix} \begin{bmatrix} x_1(k) \\ x_2(k) \end{bmatrix} + \begin{bmatrix} 0 \\ \frac{T}{m} \end{bmatrix} F(k) \\ y &= \begin{bmatrix} 1 & 0 \end{bmatrix} \begin{bmatrix} x_1(k) \\ x_2(k) \end{bmatrix} \end{aligned} \tag{4.8}$$

The potential field of the obstacle generates a repulsive force over the lateral boundaries when the distance between them is smaller than a certain threshold. The threshold is defined as a safety minimum distance between the medical staff and the robot. In this work this safety distance is defined as $d_0 = 0.5m$. The force magnitude is proportional to the square of the distance following the equation system

$$F_{rep} = \begin{cases} k_{obst} \left(\frac{1}{d_{obst}} - \frac{1}{d_0} \right) \frac{1}{d_{obst}^2} & if \quad d_{obst} < d_0 \\ 0 & if \quad d_{obst} \geq d_0 \end{cases} \tag{4.9}$$

A simulated scenario is prepared where an obstacle approaches the robot while it is performing an RMIS task to test and validate the obstacle-avoidance strategy. The staff member is represented by a cylinder with a diameter of 0.5 meters. The object approaches the robot from the

Y^+ of the robot base frame, remains at a close distance and returns. The duration of the test is $t = 5s$ with a sampling time of $T = 0.01s$. Figure 28a shows the left and right boundaries and their dynamic response when the object approaches. Figure 28b shows the repulsive force generated by the object based on the distance to the boundary.

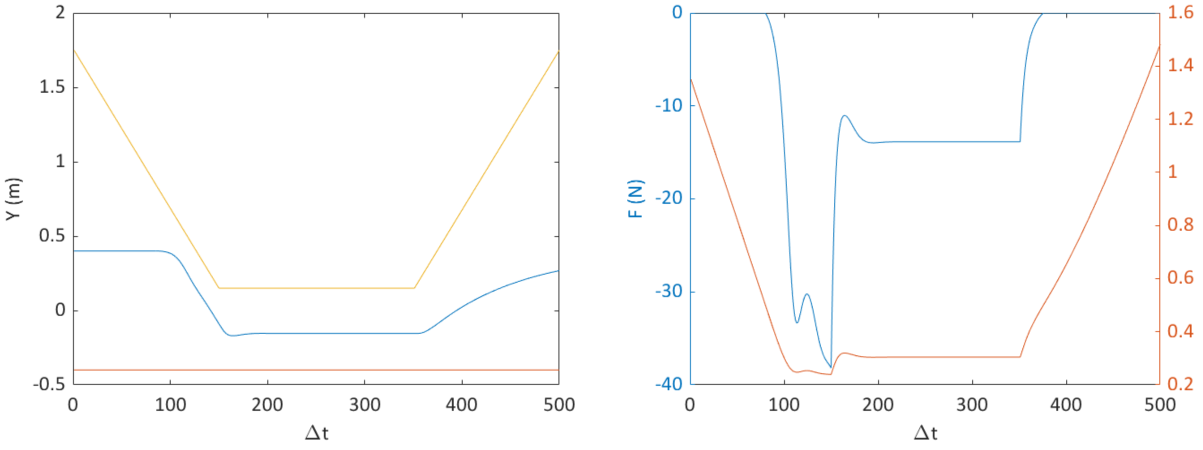

(a)

(b)

Figure 28: Results from the test of the obstacle-avoidance strategy exploiting redundancy. a) Displacement through the Y axis of the right lateral bound (red), left lateral bound (blue) and object (yellow) during the experiment duration. b) Repulsive force generated by the object (blue) and distance from the object to the left bound (red).

From the kinematics point of view, the displacement of the lateral boundaries affect the joint boundaries of q_3, which adapts to the allowed robot occupancy volume. Figure 29 shows the value of the external joint in the obstacle-avoidance experiment alongside the external joint boundaries.

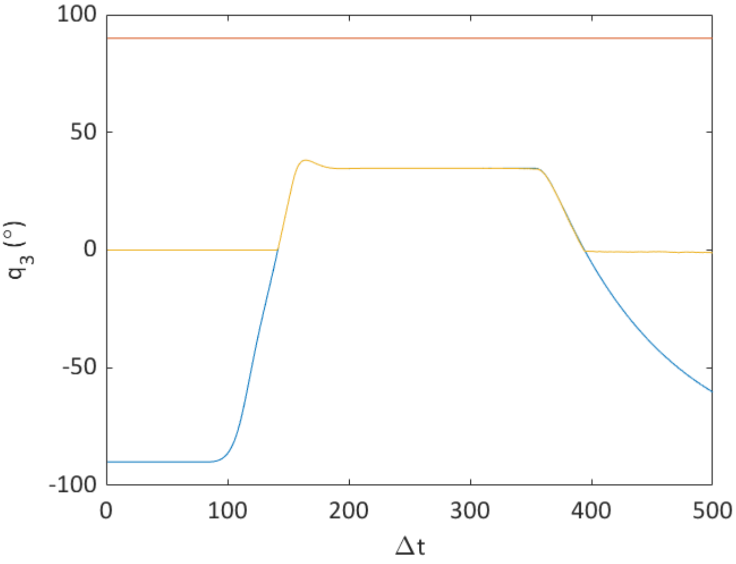

Figure 29: Changes in redundant joint value and boundaries during obstacle-avoidance experiment. The q_3 upper boundary is represented in red, the q_3 lower boundary in blue and the $q3$ value in yellow.

The results show the expected behaviour of the robot with the obstacle-avoidance policy. Left boundary moves away with a controlled motion when the object approximates and applies a repulsive force. The displacement of the left bound restricts the minimum value of q_3: from $-100°$ to almost $40°$. When the obstacle moves away, the left boundary returns to its original position and, in consequence, the lower boundary of q_3 recovers its original value. In terms of control, the hard damper and the soft spring configuration ensures that the lateral bound reacts to the object pushing force without significant overshoot, reaching fast the steady state without oscillations and returning with a smooth transition.

The same experiment is simulated again, with the dynamic manipulability optimization and the obstacle-avoidance strategy activated. Both subtasks are performed simultaneously to the main task (fetoscope tip trajectory) within their corresponding priority levels (dexterity optimization has the lowest priority). Figure 30a shows the external joint value and its boundaries along the task execution. The experiment shows the dynamic change of q_3 within the lateral bounds. Figure 30b shows the manipulability ratio between the two experiments. The results prove the validity of the proposed priority-based hierarchy control architecture using the null-space projection.

Figure 31 shows snapshots of the simulation of the obstacle-avoidance strategy exploiting the redundant joint. It can be observed that the obstacle-avoidance subtask is performed independently form the main task while the robot avoids the collision with the obstacle.

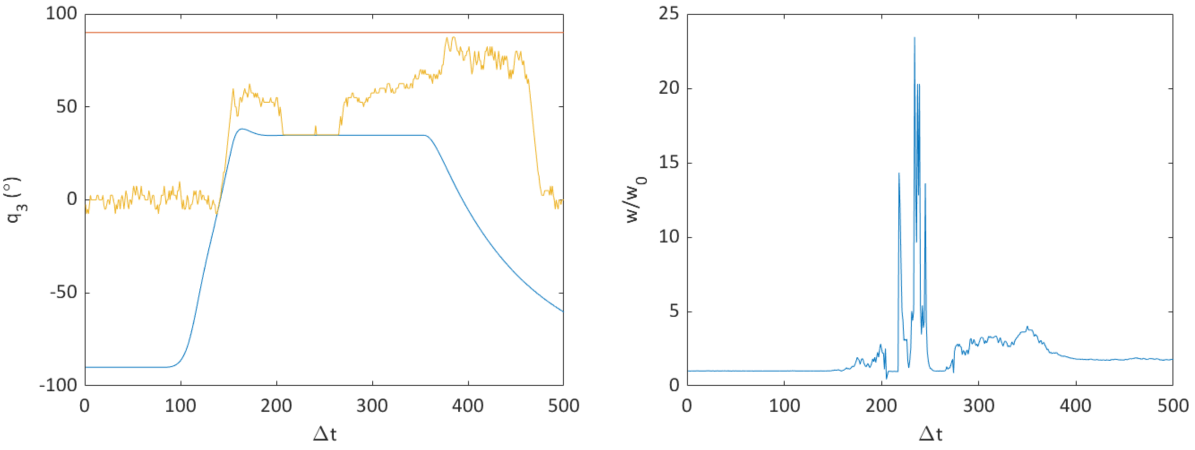

(a) (b)

Figure 30: Results of the obstacle-avoidance experiment with dynamic manipulability optimization. a) Changes in redundant joint value and boundaries during obstacle-avoidance experiment. The q_3 upper boundary is represented in red, the q_3 lower boundary in blue and the $q3$ value in yellow. b) Manipulability ratio between the two experiments, where w_0 corresponds to the previous experiment manipulability.

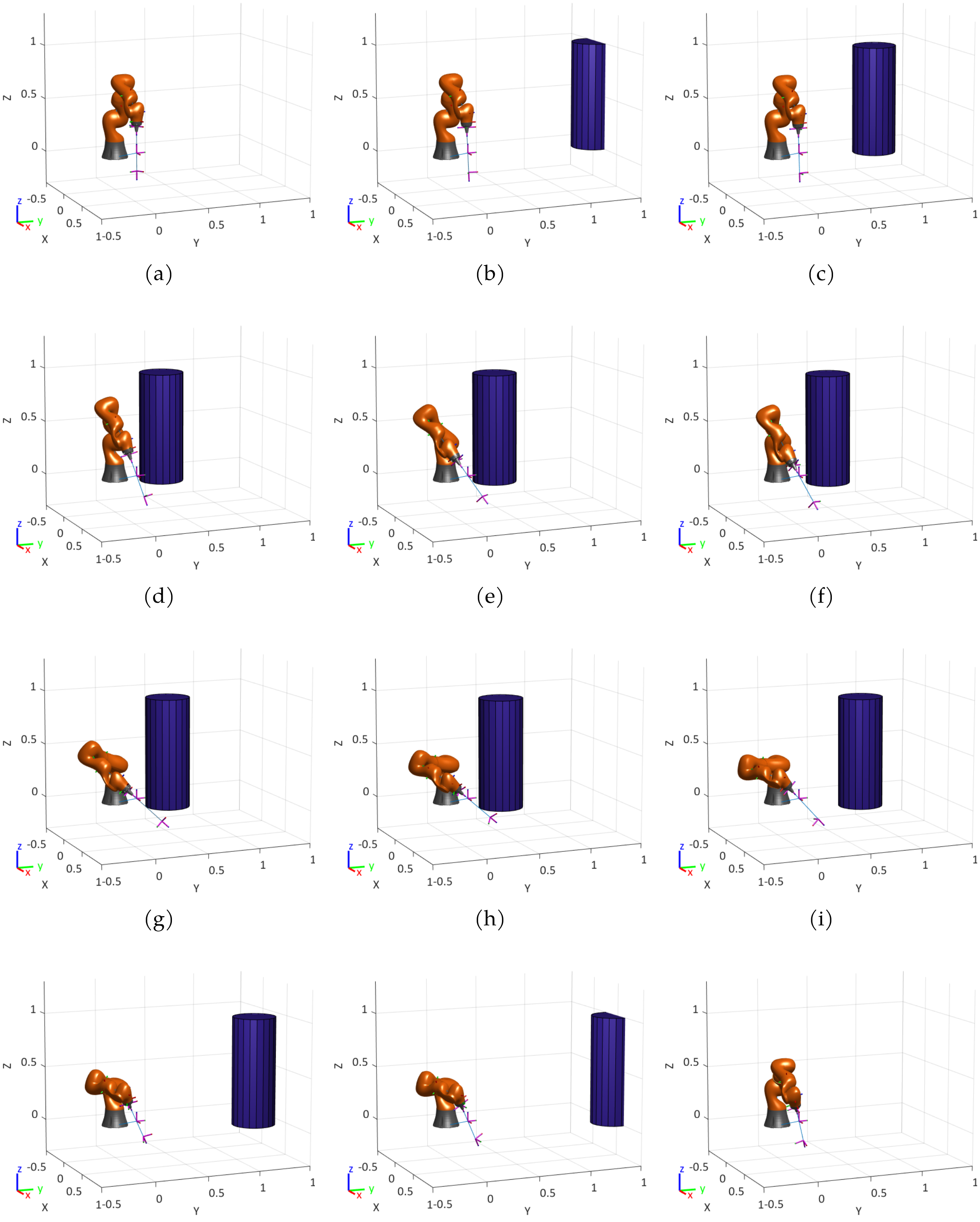

(a) (b) (c)

(d) (e) (f)

(g) (h) (i)

(j) (k) (l)

Figure 31: Example of the collision-avoidance policy exploiting redundancy applied to a redundant robot performing a RMIS task. From a) to l), snapshots in chronological order.

4.2 Compliant control strategy using null-space motion

Collaborative strategies can be used to ensure surgeons' safety when interacting with the robot. Kinematic redundancy can be exploited to integrate a collaborative control in the null-space, which do not interfere with the main task of the system (explained in eq. 2.2). A collaborative control is proposed to react with compliance on human-robot physical interaction without compromising the surgical task, thus providing a flexible workspace for the medical staff. In the proposed scenario, a surgeon needs a region of the workspace that is occupied by the robot. Without altering the TCP trajectory, the surgeon can physically push the robot arm to change its configuration in order to free occupancy volume. Moreover, compliance control can manage collisions reacting in a safe manner.

The proposed compliance control uses the integrated joint torques of collaborative robots to sense an external torque (τ_{EXT}) when the surgeon applies a force to the robot arm (F_{HRI}). This sensorization system allows to determine the exerted force on any point of the robot's geometry. The compliance control is based on an admittance controller with damping coefficient and spring stiffness as the one explained in 4.2. The spring stiffness models the opposing force to the displacement and the return of the arm robot to the original configuration after the physical interaction. Stiffness can be set for no return (zero stifness), slow return (soft stiffnes) or fast return (hard stiffness). When a force is applied, the robot configuration is displaced to the direction of the force by means of an external joint offset computed in the compliance control module. This q_3 offset is introduced in the IK solver and forces a change on the occupancy volume of the robot. Figure 32 shows the overall control scheme of the system with the main task and the compliant strategy.

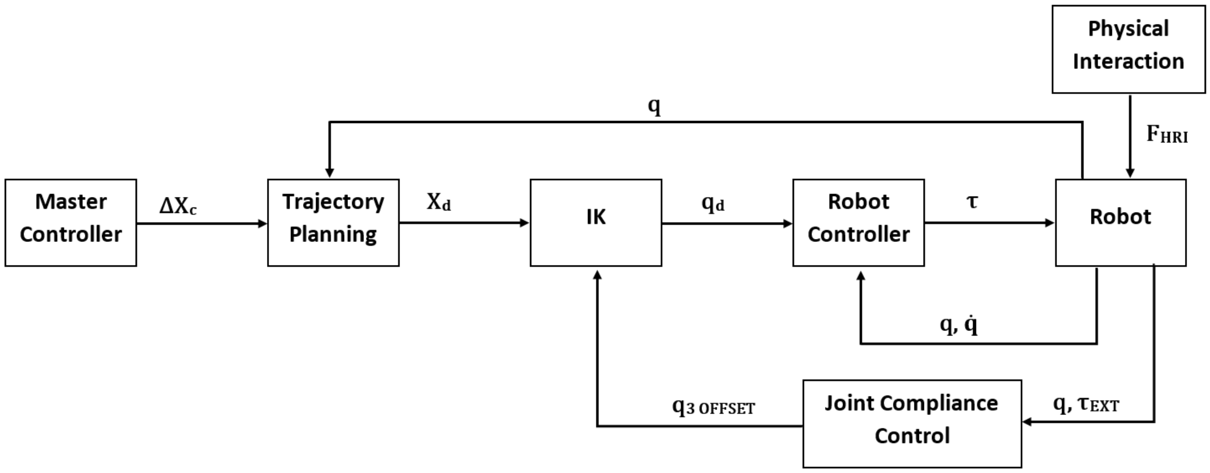

Figure 32: Control structure the collaborative compliant control subtask.

To test and validate the joint compliance control, a simulated scenario is prepared where a pushing force is applied to the robot arm while it is performing an RMIS task. Human-robot interaction is simulated by an sphere that approaches the robot, from the Y^+ of its base frame, and collides with it exerting a pushing force for a period of time. The same scenario has been simulated with two different values of stiffness for different compliant behaviours of the robot arm: zero stiffness for no return and moderate stiffness for a moderate return. The damping coefficient is the same for both simulations. The time duration of the test is $t = 5s$ with a sampling time of $T = 0.01s$.

Figure 33 shows the results of both simulations. The left column (fig. 33a,c,e) shows the results of the no stiffness compliance control, while the right column (fig. 33b,d,f) shows the the results of the moderate stiffness compliance control. Figures 33a and 33b show the force applied over the robot and the change in q_3 value for the time history. Figures 33c and 33d show the joint values in the test duration. Two dashed lines indicate the beginning and the end of the physical interaction. To verify that the compliance control does not affect the main task, the trajectory error of the TCP is analyzed during the physical interaction. Figures 33e and 33f show the distance error in the Cartesian space between the real TCP position, computed with FK, and the desired position of the trajectory. Again, two dashed lines indicate the beginning and the end of the physical interaction.

The results of the experiment show the expected behaviour of the proposed compliant control. When a force is exerted on the robot, the external joint value changes in a controlled manner. This causes a change of the robot configuration in the null-space, which can be permanent or not depending on the stiffness parameter of the compliant control. The lack of significant deviations in the position error of the TCP validate the effectiveness of the projection of the compliance control into the null-space. The stiffness parameter changes the behaviour of the manipulator configuration when the force ceases. In future research, a dynamic stiffness parameter will be studied to react properly to different interactions (e.g. accidental collision, deliberate push). This stiffness parameter would be time-variant in function of the force exertion duration. Given a physical interaction, the dynamic stiffness start at a high level and decreases its value toward zero as the force is continued. Following this approach, for a accidental collision of short duration, the high stiffness makes the robot return to the original position. On the contrary, if the surgeon wants to free the working space pushing the robot to the other side, the force exertion can be maintained over a few seconds to let the stiffness reach zero.

The simulations to test the compliance can be observed in figures 34 and 35. Both figures show various snapshots of the simulation. The sphere that represents the physical interaction is colored in red when there is a force exertion over the robot and in green when there is no force applied. Figure 34 shows the compliance control with no return while figure 35 shows the compliance control with return.

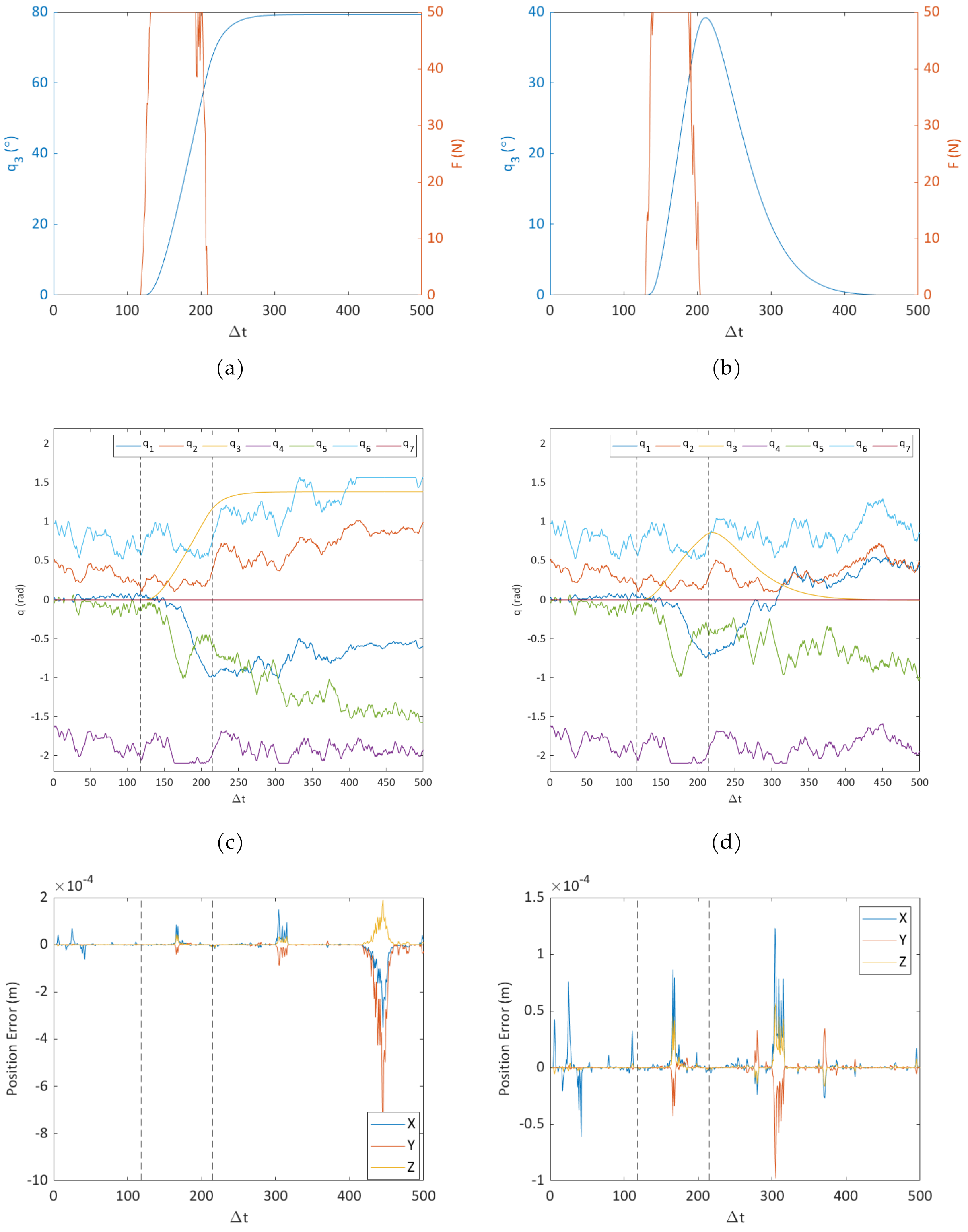

(a) (b)

(c) (d)

(e) (f)

Figure 33: Results from the joint compliance strategy exploiting redundancy. Left column: Compliance control with no stiffness. Right column: Compliance control with moderate stiffness. a,b) Force exerted over the robot arm (red) and variation of the joint value of q_3 (blue). c,d) Joint values for the time duration of the experiment, with dashed lines that marks the beginning and the end of the physical interaction. e,f) TCP position error in the Cartesian, with dashed lines that marks the beginning and the end of the physical interaction.

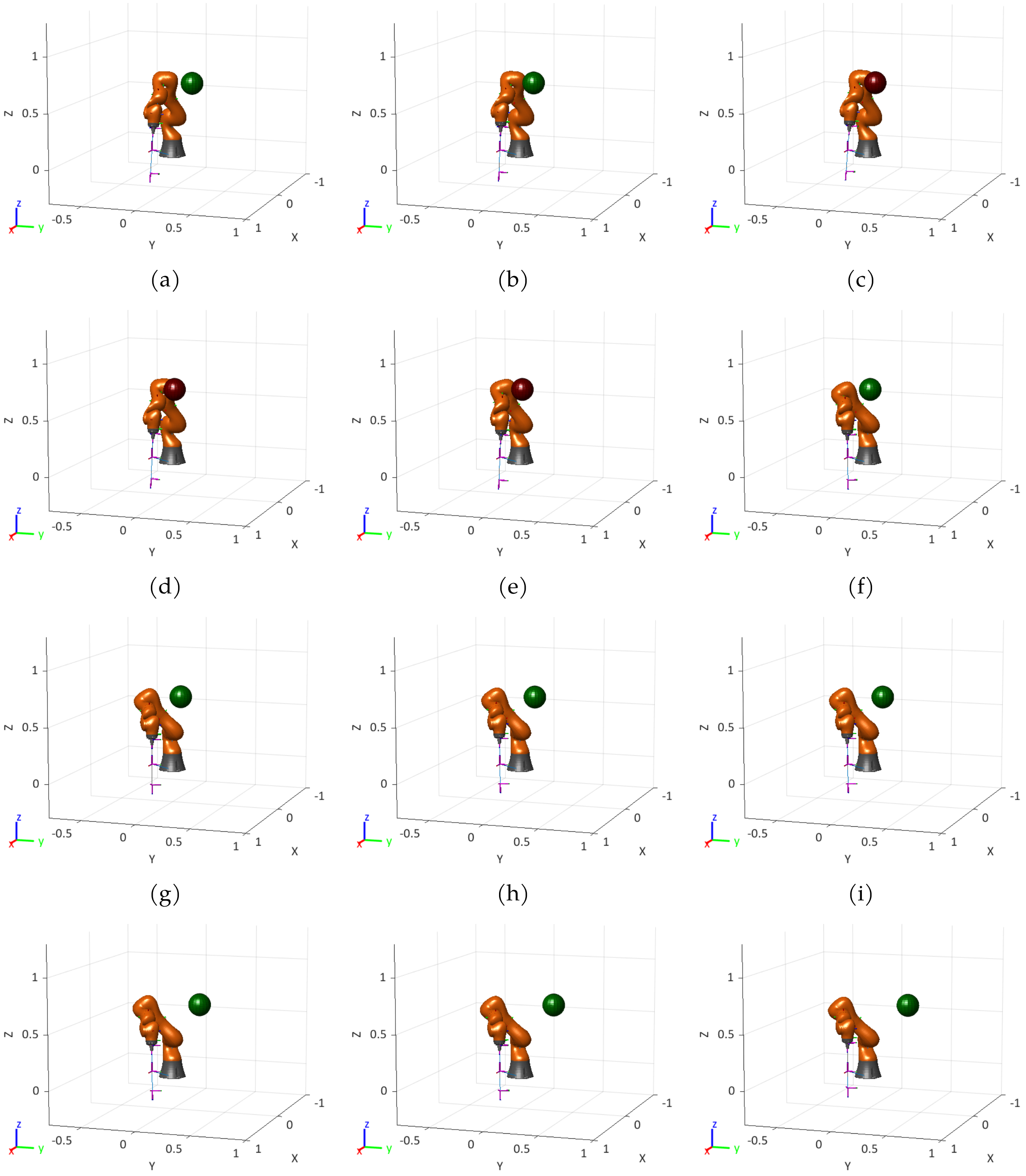

(a) (b) (c)

(d) (e) (f)

(g) (h) (i)

(j) (k) (l)

Figure 34: Compliant control exploiting null-space motion for human-robot interaction. Compliant control with no return (soft damper and no spring). Red sphere indicates physical contact.

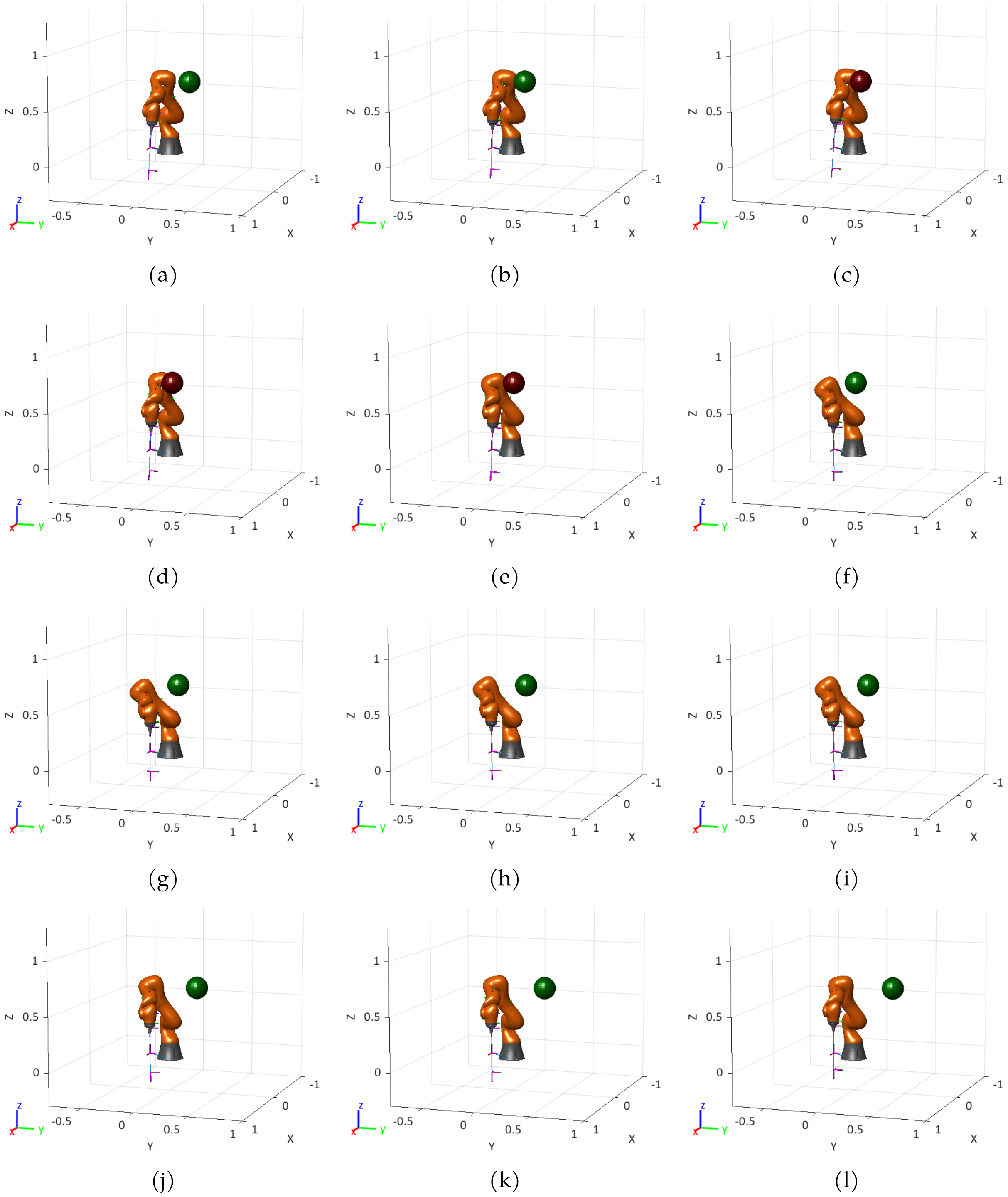

(a) (b) (c) (d) (e) (f) (g) (h) (i) (j) (k) (l)

Figure 35: Compliant control exploiting null-space motion for human-robot interaction. Compliant control with return (soft damper and soft spring). Red sphere indicates physical contact.

4.3 Co-manipulation control strategy for manual operation.

Robotic teleoperation in RMIS has proven benefits in terms of precision, safety, dexterity, etc. On the contrary, RMIS requires long setups, penalizing the surgical execution time and, consequently, the surgical room performance. This drawback translates directly into higher economic costs and less implantation of robotic systems inside the surgical room. The pre-operatory setup and post-operatory removal of the robot can be optimized with manual operation of the robot through co-manipulation. Co-manipulation is a collaborative approach that allows the surgeon to control the robot through manual guidance. Following the multi-task approach, the co-manipulation control is treated as a task with the highest priority, complementary to the teleoperated control, and performed in the task-space (see fig. 12).

A common approximation for co-manipulation control is the Computed Torque Method [38]. This method controls the robot via joint computed torques with the inverse dynamics model

$$M(q)\ddot{q} + C(q,\dot{q})\dot{q} + g(q) - \tau_{EXT} = \tau \tag{4.10}$$

where $M(q) \in \mathbb{R}^{n \times n}$ is the inertia matrix, $C(q,\dot{q}) \in \mathbb{R}^n$ is the Coriolis and centrifugal effects, $g(q) \in \mathbb{R}^n$ is the gravity force on the robot, $\tau_{EXT} \in \mathbb{R}^n$ represents the external torques exerted on the robot and $\tau \in \mathbb{R}^n$ the control internal torques.

This control method is optimal for low-level control and is commonly used (e.g. in [43]-[44]) as it does not change the physical magnitude between the input and output (both forces). However, the HATTTS teleoperated system operates on a higher control layer with a position-based control. Therefore, a different approach to the torque control is needed to implement the co-manipulation strategy.

The proposed co-manipulation control is based on an admittance controller, a commonly used position-based control method in HRI. The admittance controller, defined in eq. 4.2, transforms an input force into a position displacement of the controlled device with damped and stiffness behaviour. The implemented co-manipulation control (fig. 36) uses the integrated end effector force sensor of the collaborative robot (KUKA LWR) to sense the external forces (F_{EXT}) exerted by the surgeon when moving the end effector manually (F_{HRI}). The force sensor measures any applied external force and torque on the end effector ($F_X, F_Y, F_Z, F_{Roll}, F_{Pitch}, F_{Yaw}$). The co-manipulation control computes the new Cartesian pose of the end effector in the direction of the force and torque. Equation 4.11 defines the adapted admittance control used for co-manipulation, where the stiffness parameter is null as free motion is desired.

$$M\ddot{X} + D\dot{X} = F_{EXT} \tag{4.11}$$

where $M \in \mathbb{R}^{n \times n}$ and $D \in \mathbb{R}^{n \times n}$ are the mass matrix and the damping matrix respectively. To compute the displacement X, the implicit Euler discretization (see equation 4.7) is used in the differential equation 4.11. The new Cartesian pose of the end effector Xd, given by the forced displacement, is sent to the IK solver to compute the robot configuration. The result of the co-manipulation control is a passive behaviour of the robot. Moreover, the admittance control can be constrained to a singular axis of motion. For example, for the tool insertion and extraction the admittance control can be restricted to the Z axis of the tool. The Z_{Tool} movement constrain is useful to insert and guide the fetoscope inside the trocar during the set-up pre-operative phase. The same schema can be applied to extract the fetoscope during the post-operative phase.

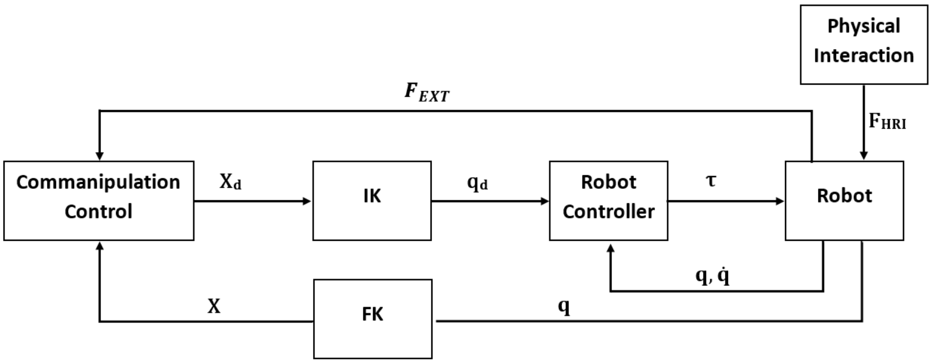

Figure 36: Control structure for the co-manipulation collaborative strategy

The co-manipulation control has been tested in simulation. The robot starts in a given position $q_i = \begin{bmatrix} 0 & \pi/18 & 0 & -\pi/12 & 0 & \pi/3 & 0 \end{bmatrix}$. As the manual guidance can be difficult to model, the physical interaction is simulated with a force and torque vector over the end effector. The simulation has a duration of $t = 2s$ with a sampling time of $T = 0.01s$. Figure 37a shows the value of the force vector over time. Figure 37b shows the joint values of the manipulator for the test duration.

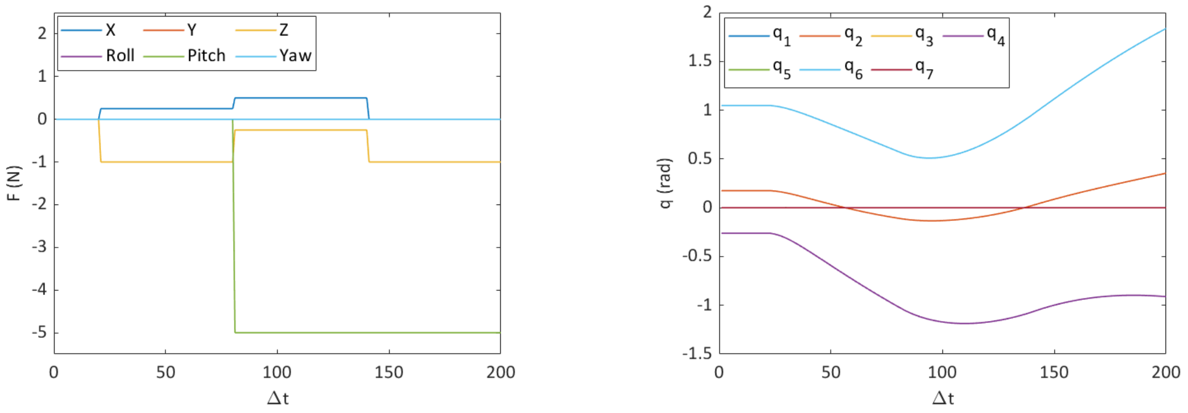

(a) (b)

Figure 37: Results from the test of the co-manipulation strategy. a) External forces and torques exerted on the tool tip. b) Joint values.

In the real system, the force measures are filtered by the control to avoid hand tremor. Additionally if the system receives a force vector with an opposite direction as the previous one, the control stores the force vector without applying it. In the next step, if the new force vector received has the same direction as the stored one, the stored vector is then introduced into the control. This approach is useful to avoid noise in the force lecture and perform a continuous motion. The force vector is on hold just for a sampling time period. Excessive delay in the force application causes a loss in the user sensation of control.

Figure 38 show various snapshots of the simulation of the co-manipulation strategy. The external force vector is represented with a red arrow. External pitch torque is not represented.

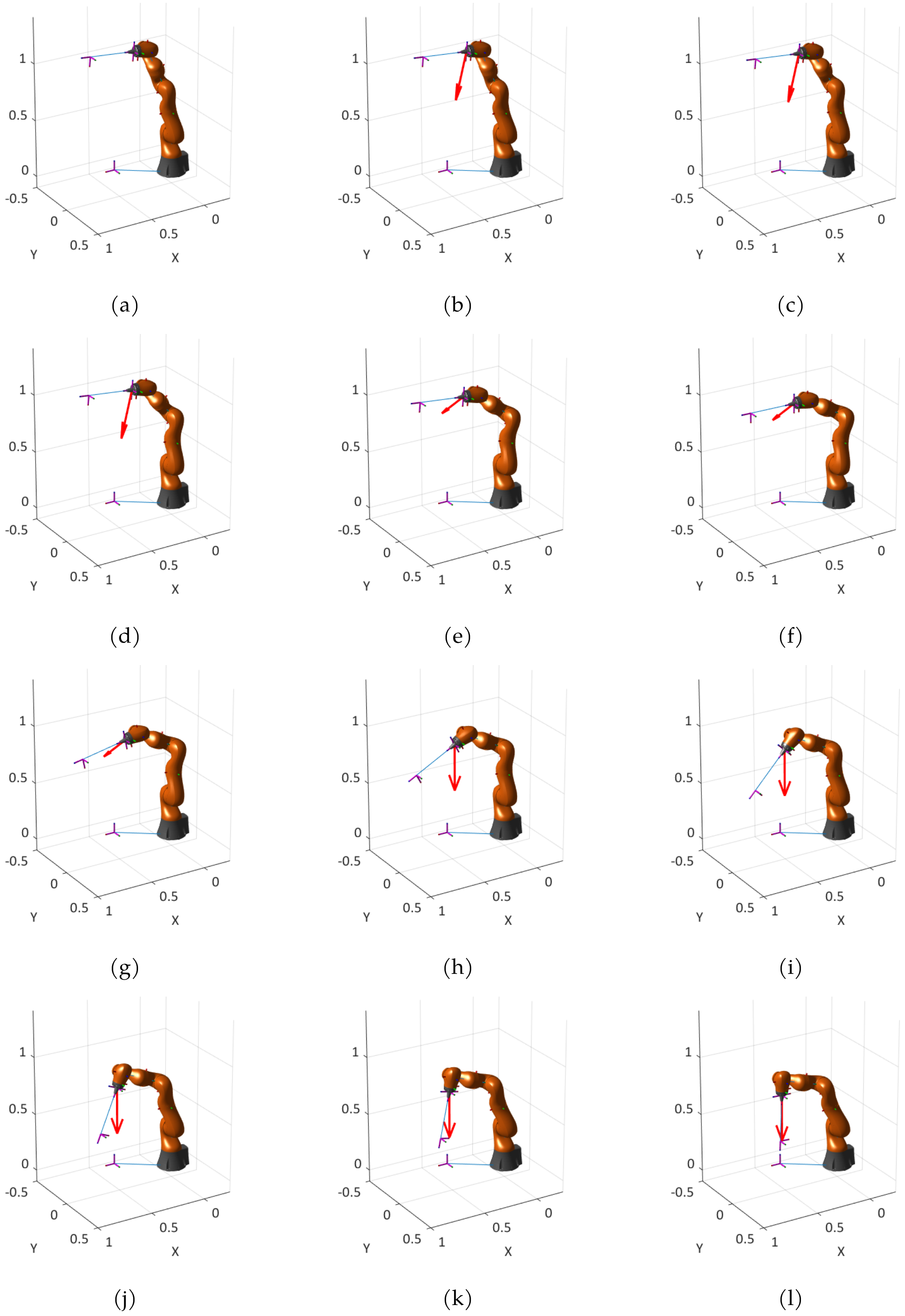

(a) (b) (c)

(d) (e) (f)

(g) (h) (i)

(j) (k) (l)

Figure 38: Co-manipulation control for physical guidance of the robot. The red arrow indicates the force vector exerted on the end effector.

5 Integration of a KUKA LightWeight Robot in HATTTS

This section describes the integration of a KUKA LWR4 in the HATTS teleoperation platform. The current platform uses an Staübli RX60b, a industrial 6 DoF serial robot, in the slave station. This robot presents several limitations in terms of reachable workspace, dexterity and lack of compliant capabilities. All these restrictions generated the need of a redundant and compliant robot. The KUKA LightWeight Robot 4 is a valid solution to the system requirements. The proposed new robot is a redundant and collaborative robot that will allow the integration of the developed multi-task control strategy.

The KUKA LightWeight Robot (fig. 39) is a 7 DoF serial manipulator developed through a research collaboration between the German Aerospace Center (DLR) and KUKA Roboter. The partnership between KUKA and DLR began in 1991 with the concept of a small lightweight robot with a weight-to-payload ratio of 1:1, contrary to the heavy standard robots at that time. The KUKA LWR 4 is the fourth generation lightweight robot, with major characteristics like kinematic redundancy, anthropomorphic arm-shape, torque measurements in all joints, programmable compliance at joint and Cartesian levels and active vibration damping [45].

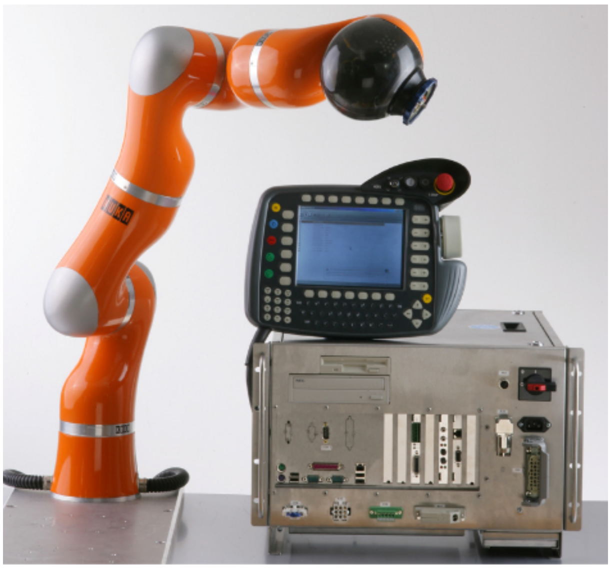

Figure 39: The Kuka LightWeight Robot 4 with KUKA Robot Controller (KRC) and KUKA control panel (KCP)

5.1 Advantages of KUKA LightWeight Robot 4

This section offers a comparison between the current robot in the HATTTS system, a Staübli RX60b, and the KUKA LWR4. Table 1 shows a comparison of the main features between the two robots. Unlike the Staübli RX60b, the KUKA LWR4 is a 7DoF redundant robot that offers a workspace according with the FLP surgical requirements. The disposition of the robot together with the RCM and the working space causes the Staübli to easily fall into singularities and joint limits. The result is a limited workspace and, consequently, a limited applicability in real scenarios. Redundancy avoids the LWR4 to fall in singularities and reach joint limits. Apart from the kinematic redundancy, other characteristics of the KUKA LWR4 are interesting. The KUKA LWR has integrated torque sensors in each joint, enabling the implementation of collaborative control strategies.

Regarding the implementation of the platform in the operating room, the monophasic power supply of the KUKA LWR4 allows the robot to enter in a surgery room, since it is forbidden by regulation the use of any electrical system powered at 400 V, as required for Staübli robot. In previous phases of the project, this was one of the main reasons why it was not possible to start the experimentation on animals. Also, the reduced weight facilitates the transport and implantation in the operating room.

Table 1: Comparison of main features of KUKA LWR4 and Staübli RX60B

Feature	**Staübli RX60b**	**KUKA LWR 4**
Num. DoF	6	7
Max. Payload	4.5 kg	7 kg
Weight	44 kg	15 kg
Repeatability	± 0.02 mm	± 0.05 mm
Integrated Torque Sensors	No	Yes
Power Supply	400 V	220 V

The loss of repeatability due to robot replacement does not affect the system, since the requirements in this respect are much lower (± 0.5 mm is considered enough). Besides, the variation of the RCM and the flexibility of the fetoscope causes a loss of accuracy. However, the control loop of the tool positioning is done by the user's vision in free navigation mode or by computer vision when automatic precision adjustment is needed (e.g. relocation and anastomosis).

5.2 Software integration

The integration of the KUKA LWR4 into the HATTTS system is done using the Fast Research Interface (FRI) library. The FRI interface gives direct low-level real-time access to the KUKA robot controller from an external system. The FRI interface is composed of a C++ library, for the external computer, the KUKA Robot Language (KRL) library and drivers for the KUKA Robot Controller (KRC) The KUKA KRL is the proprietary programming language used to control KUKA robots. The KUKA KRC is the universal controller unit for all KUKA robots. Figure 40 shows an overview of the system architecture.

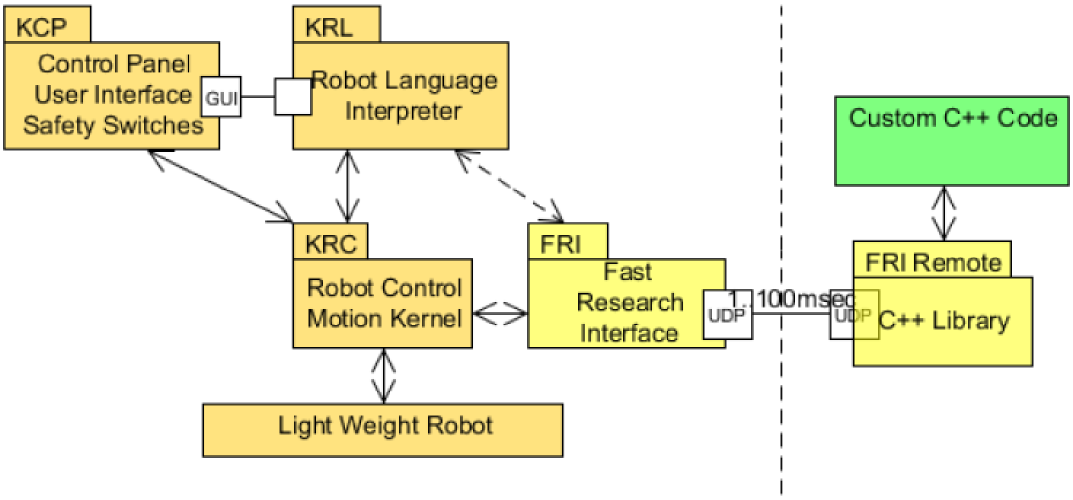
KCP
Control Panel
User Interface
Safety Switches
GUI
KRL
Robot Language
Interpreter
Custom C++ Code
KRC
Robot Control
Motion Kernel
FRI
Fast
Research
Interface
UDP
1..100msec
UDP
FRI Remote
C++ Library
Light Weight Robot

Figure 40: Diagram of FRI control architecture. Figure source from [45].

Based on Ethernet UDP protocol, the FRI interface allows the user to control the robot and monitor its status from an external PC. When a external computer establishes a FRI connection to the KRC, the monitor mode allows the reception of the robot status data (e.g. joint angle, Cartesian position, external torque) whereas the command mode allows to send control commands to the robot (fig. 41). To ensure safety, the FRI interface measures the quality of the communication between the external computer and the KRC and restricts the command mode if its not suitable. (fig. 42).

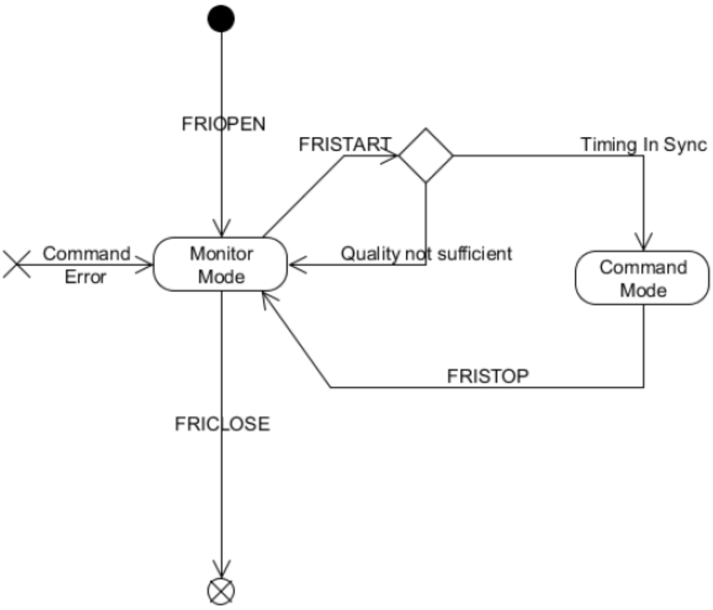
FRIOPEN
FRISTART
Timing In Sync
Command Error
Monitor Mode
Quality not sufficient
Command Mode
FRISTOP
FRICLOSE

Figure 41: State machine for FRI monitor and command mode. Figure source from [46].

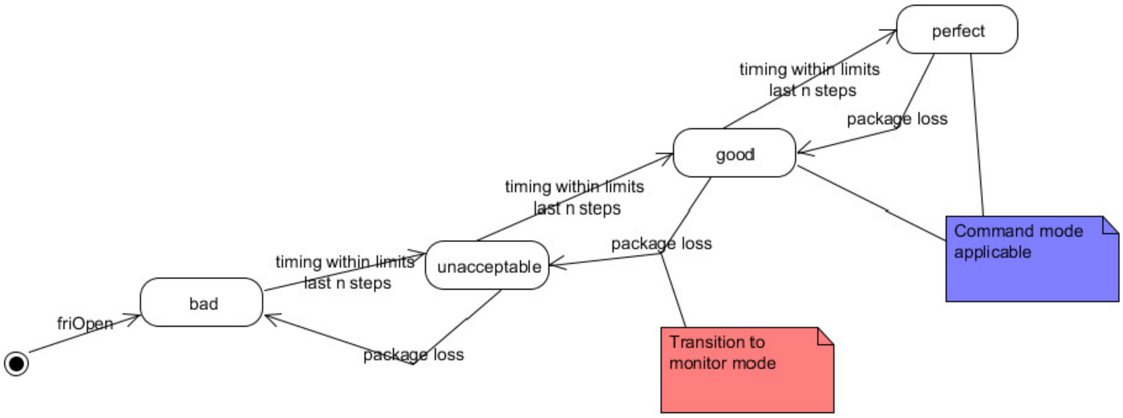
perfect
timing within limits last n steps
package loss
good
timing within limits last n steps
Command mode applicable
package loss
timing within limits last n steps
unacceptable
bad
friOpen
package loss
Transition to monitor mode

Figure 42: State machine of the data transfer quality and the allowed modes. Figure source from [46].

The FRI library has been dealt with in the laboratory before. In a previous project, an application was developed that simulated the KUKA teach pendant using FRI. From the graphical user interface of this application (fig. 43), the robot can be moved by setting joint values or Cartesian positions, the user can set the stiffness and damping parameters for the Cartesian or Joint impedance control and virtual forces and torques can be generated. This application has been used as reference when using the FRI library.

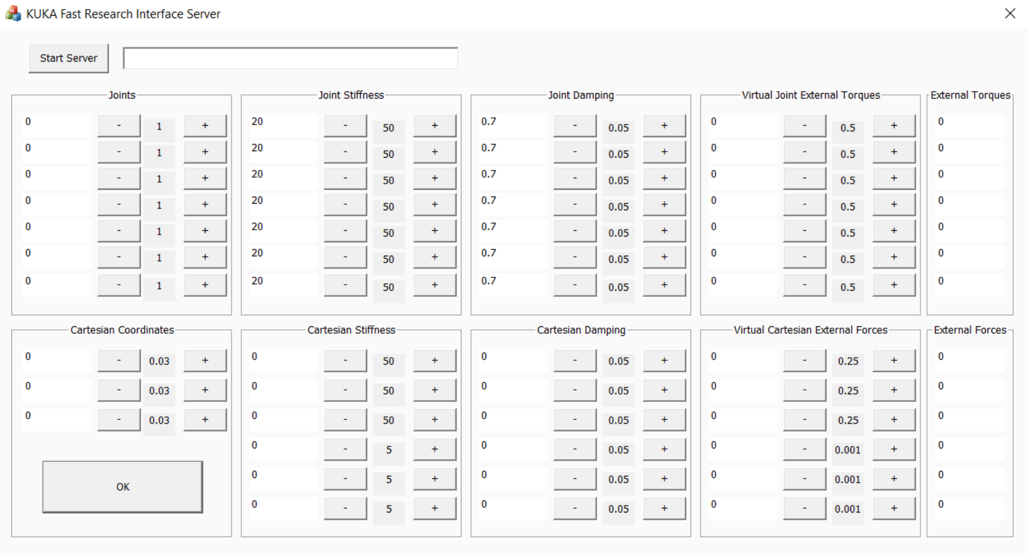

Joints			
0	-	1	+
0	-	1	+
0	-	1	+
0	-	1	+
0	-	1	+
0	-	1	+
0	-	1	+

Joint Stiffness			
20	-	50	+
20	-	50	+
20	-	50	+
20	-	50	+
20	-	50	+
20	-	50	+
20	-	50	+

Joint Damping			
0.7	-	0.05	+
0.7	-	0.05	+
0.7	-	0.05	+
0.7	-	0.05	+
0.7	-	0.05	+
0.7	-	0.05	+
0.7	-	0.05	+

Virtual Joint External Torques			
0	-	0.5	+
0	-	0.5	+
0	-	0.5	+
0	-	0.5	+
0	-	0.5	+
0	-	0.5	+
0	-	0.5	+

External Torques
0
0
0
0
0
0
0

Cartesian Coordinates			
0	-	0.03	+
0	-	0.03	+
0	-	0.03	+

Cartesian Stiffness			
0	-	50	+
0	-	50	+
0	-	50	+
0	-	5	+
0	-	5	+
0	-	5	+

Cartesian Damping			
0	-	0.05	+
0	-	0.05	+
0	-	0.05	+
0	-	0.05	+
0	-	0.05	+
0	-	0.05	+

Virtual Cartesian External Forces			
0	-	0.25	+
0	-	0.25	+
0	-	0.25	+
0	-	0.001	+
0	-	0.001	+
0	-	0.001	+

External Forces
0
0
0
0
0
0

Figure 43: Graphic user interface simulating the KUKA LWR teach pendant using FRI. Available at the laboratory prior to this project.

As each robot has its own programming language and requires different protocols in communications and data processing, the replacement of the slave robot is not immediate. The main control module of the system must be adapted to match the new robot communication protocol. The solution proposed relies on the development of an intermediary software layer, between the HATTTS central control module and the KUKA controller. This intermediary software gives an abstraction layer that works as an interpreter, managing the data exchange between the robot and the system and adapting the data bus to the communication protocol of each system. Figure 44 shows a scheme representation, based on the communications scheme of the HATTTS system shown in figure 6, of the integration of the KUKA LWR4 with the intermediate layer into the control architecture of HATTTS. This solution has been used in previous projects, enabling the use of different robots without the need of altering the developed high level controls or programming dedicated software specific for each robot. The interpreter is already implemented for the Staübli and ABB robots of the laboratory. The new version of interpreter incorporates the stiffness control and the 7DoF joint control of the robot.

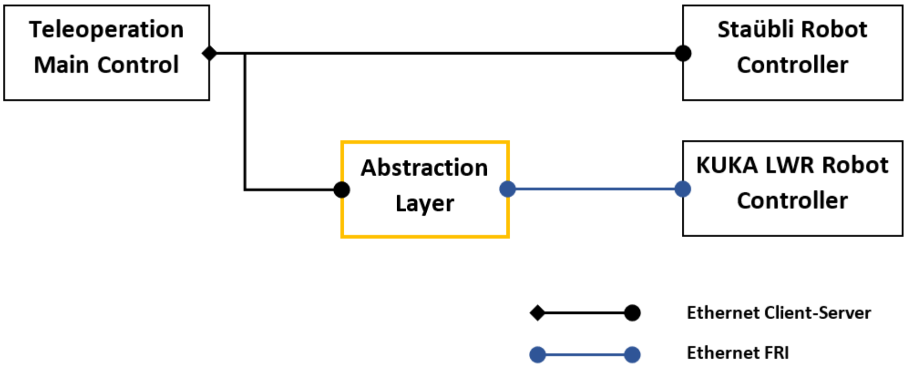

Figure 44: Integration of the KUKA LWR4 into the control architecture of the HATTTS system using a intermediary abstraction layer

Following the client-server structure of the control architecture of HATTTS, the interpreter is integrated as a server module running in a PC with Ethernet connection to both the central control module and the robot controller. The interpreter module has a dialog-based GUI developed in Visual Studio 2017. This GUI gives information of the status of the module (e.g. connection succeeded, errors), the robot (e.g. joint values, Cartesian position, external torques), the FRI connection (e.g. status, quality, power, control mode) and the server socket (e.g. status, client address, server address, port). The information is presented together with a color code, for a quick understanding of the overall status. The FRI status shows red when is closed, blue in monitor mode and green for command mode. The server socket shows red when is closed, blue when is open and green when a client is connected. The quality of the FRI communication shows red when is "unacceptable", orange when is "bad", light green when is "OK" and dark green when is "perfect". The power shows green when the robot has the motors power enabled and red otherwise. Behind the user interface, a multi-thread process handles the communication between the two systems. Figure 45 shows a snapshot of the developed GUI for the interpreter server.

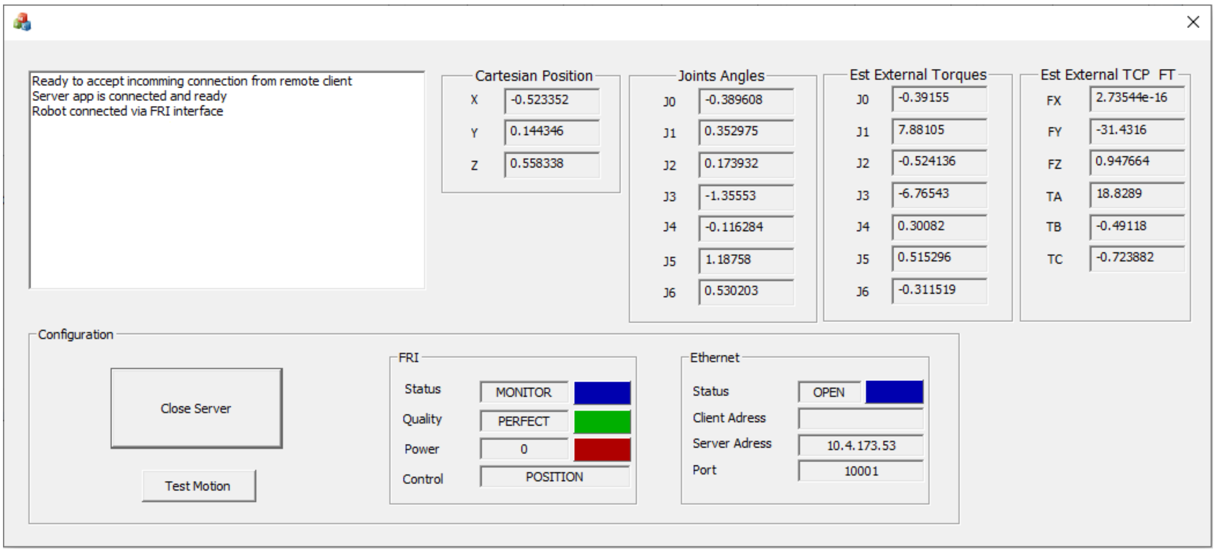

```
Ready to accept incomming connection from remote client
Server app is connected and ready
Robot connected via FRI interface
```

Cartesian Position	
X	-0.523352
Y	0.144346
Z	0.558338

Joints Angles	
J0	-0.389608
J1	0.352975
J2	0.173932
J3	-1.35553
J4	-0.116284
J5	1.18758
J6	0.530203

Est External Torques	
J0	-0.39155
J1	7.88105
J2	-0.524136
J3	-6.76543
J4	0.30082
J5	0.515296
J6	-0.311519

Est External TCP FT	
FX	2.73544e-16
FY	-31.4316
FZ	0.947664
TA	18.8289
TB	-0.49118
TC	-0.723882

FRI		
Status	MONITOR	🟦
Quality	PERFECT	🟩
Power	0	🟥
Control	POSITION	

Ethernet		
Status	OPEN	🟦
Client Adress		
Server Adress	10.4.173.53	
Port	10001	

Figure 45: Graphic user interface for the interpreter module.

The interpreter connection to the central control module is done using a TCP/IP server socket using the *winsock2.h* library. The central control module connects to the interpreter module as a client and sends and receives data as string vectors. The command string vector have a fixed length and contain in the first position an integer that corresponds to a code ID. This code number indicates the control action to perform, which can be motion (e.g. incremental Cartesian, incremental joints, absolute Cartesian, incremental in tool axis) or communication (e.g. open connection, close connection, reset). In order to ensure that the data package has not been corrupted, the command vector has a last value that corresponds to the checksum. The checksum value is the sum of the data vector multiplied by the code ID. When the interpreter receives a message from the central control module, first decodes the control action and then performs the checksum. If the checksum is equal to the one in the data vector the package has not been corrupted and the command action is performed. The interpreter replies to the central control module with a data vector that contains the robot pose, the joint values, the external joint torque and the external TCP force and torque. The received motion commands are defined position or joint goals. In case of incremental motion, the goal is calculated from the position data received from the robot plus the increment. The communication protocol follows the specification of previous interpreters ensuring the compatibility with previous versions.

The major inconvenience is that the FRI library defines the Cartesian pose from the homogeneous transformation matrix of the end effector $[R_{3\times3}P_3]$, whereas the central control module defines the Cartesian pose with the position and the set of Euler angles ZYZ. The interpreter manages the conversion of the Cartesian pose representation.

The FRI thread manages the communication with the robot. The FRI library provides an update function that sends a command data vector and receives a robot data vector. When the central control unit communication thread sets a position goal, the FRI thread calculates in each step the error between the current and goal poses. To ensure smooth robot movements, the interpreter imposes a maximum step increment (0.001 rad/step) and divides the motion in a number of sub-steps equal to the maximum individual error divided by the step increment. This allows the robot reach all the components of the goal pose or joint configuration in coordination.

The interpreter module starts the application opening a FRI connection with the KUKA LWR4. If the quality of the FRI connection is good, then the application opens a server socket. The central control module connects to the interpreter server socket as a client. If the FRI connection is in monitor mode, the central control is informed that it cannot send commands and only receives the state of the robot. If the FRI connection is in command mode the interpreter accepts the motion commands from the central control module. If the robot's power is on, the motion commands are performed by the robot. The state machine of the interpreter module is shown in figure 46.

The interpreter module has been tested and validated to check its correct operation. From the interpreter module, the robot has been moved through the FRI library while collecting the robot's data. The TCI/IP server-client connection and communication has also been validated, receiving the messages, decoding and replying the robot's state data and error information. The last test consisted in receiving of a motion command from the client, the execution on the robot and the reply with status information. This last test was also successful and the interpreter module was considered operational.

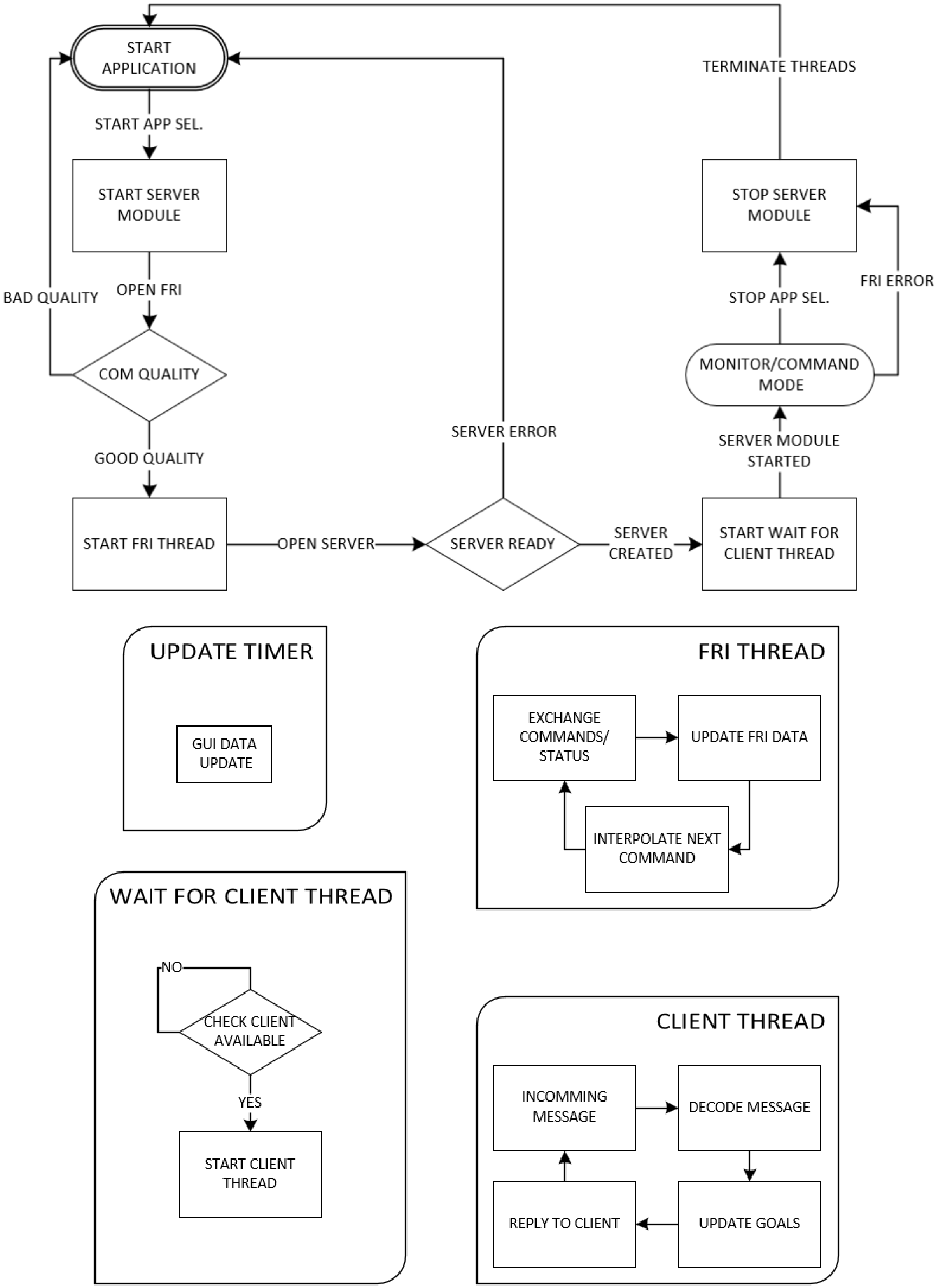
START APPLICATION
START APP SEL.
START SERVER MODULE
OPEN FRI
BAD QUALITY
COM QUALITY
GOOD QUALITY
START FRI THREAD
OPEN SERVER
SERVER READY
SERVER ERROR
SERVER CREATED
START WAIT FOR CLIENT THREAD
SERVER MODULE STARTED
MONITOR/COMMAND MODE
STOP APP SEL.
FRI ERROR
STOP SERVER MODULE
TERMINATE THREADS
UPDATE TIMER
GUI DATA UPDATE
FRI THREAD
EXCHANGE COMMANDS/ STATUS
UPDATE FRI DATA
INTERPOLATE NEXT COMMAND
WAIT FOR CLIENT THREAD
NO
CHECK CLIENT AVAILABLE
YES
START CLIENT THREAD
CLIENT THREAD
INCOMMING MESSAGE
DECODE MESSAGE
UPDATE GOALS
REPLY TO CLIENT

Figure 46: Finite State Machine representation of the interpreter module.

6 Project Budget

This section presents the budget needed to develop this project. The duration of this project has been around six months. It is not expected from this project's work a direct profit, but an advance in research that can lead, in a future, to develop a commercial platform for FLP by means of technology transfer.

Table 2 lists the items needed during the development of the project, with a brief description and its estimated price. The actual cost has been calculated as the proportional part of the total cost based on usage time (6 months). For non-current assets like the robot, laboratory installations and medical equipment, the cost calculation considers depreciation at 5 years.

Table 2: Project budget.

Item	**Desciption**	**Full Price €**	**Cost €**
HATTTS	Robotic assisted surgical teleoperation platform	*	*
Robot	KUKA LWR 4	30.000	3.000
Software	Development tools annual license (Matlab, Visual Studio, ...)	2.500	1.250
Laboratory installations	Office, laboratory equipment, supplies and workstation	12.000	1.200
Researcher	Robotics Engineer student annual salary	15.000	7.500
Medical equipment	Fetoscope, trocar, placenta phantom	20.000	2.000
Total		79.500	14.950

* The current system is the result of several projects that have evolved over the last 10 years and it is not possible to calculate a specific cost.

7 Project impact

This section briefly discusses the impact of this project in the society, the economy and the environment.

The HATTTS teleoperated platform is a novel robot-assisted surgery system with notable improvement in patient safety. The robot-assisted surgery decreases the procedure duration, reducing the exposure of the patient (mother and fetus) to anesthesia. The system optimizes the localization and proper coagulation of the anastomosis at the same time that reduces the placenta coagulated area. Moreover, the teleoperation system improves the ergonomics of the main surgeon, and consequently, the precision of movements reducing the collision risk.

Furthermore, the HATTTS system can ease the introduction of fetal surgical techniques in hospitals that do not perform this procedures. The system reduces the complexity of the procedure and the required skills. The overall work done in this project enhances the capabilities of the HATTTS system and takes it closer to the operating room. The future use of this system or other similar systems will directly benefit society by saving lives of at-risk fetuses.

The contribution of this work to the HATTTS project is based on the incorporation of a redundant and collaborative robot and the different control strategies that allow exploiting the benefits of the robot. The improvement in dexterity decrease the probability of damages on the fetus or the uterus that can require re-interventions or longer hospital stays and recovery times. The co-manipulative strategy decreases the required operating room time with an agile set-up and removal process, reducing the cost of the procedure.

Regarding the environmental impact of the project, the development of this work has required a significant amount of electricity. The energy consumption has come mainly from the use of the KUKA LWR, and also from the large number of simulation computation sessions. The future use of the teleoperation platform in the surgery room will lead to a major electrical power consumption. However, the reduction of the surgery time decreases the use of the rest of electrical systems used in the procedure.

8 Future Work

Due to the closing of university installations, for the general Covid-19 lock down, this project has been deprived of the possibility to test the developed work into the real system. Although the integration of the KUKA LWR4 into the system has been done, the test of the developed control strategies with the new robot was not possible. The first task, that will be developed immediately after the conclusion of the lock down, will be the implementation of the developed control into the real system. Secondly, an experimental phase to test the control modules in the real system will began. The surgeons involved in the project will test and validate the usefulness of the proposed control schemes in simulated surgery. Once obtained the validity in dry lab, a new phase of the project will began with the execution of tests in animals. The animal tests will be carried out in the animal facilities of the Bellvitge hospital, where they have been held previously.

Furthermore, part of the work developed in this project is intended to be presented as a conference paper in the oncoming Conference on New Technologies for Computer and Robot Assisted Surgery (CRAS 2020).

9 Conclusions

Robotic Minimally Invasive Surgery is a well established technique that improves safety, precision and control in surgery. This work presents the integration of a set of improvements at a high level of control for a robot-assisted surgery teleoperation system oriented to FLP. This improvements are based on the use of a redundant and collaborative robot to optimize the dexterity of the robot and the safety and agility of the procedure.

This work has improved this teleoperation surgery system proposing a multi-task control approach to implement secondary tasks that benefit the system in terms of dexterity and human-robot interaction. This multi-task approach is based in the exploit of kinematic redundancy to perform subtasks in the null-space, without interfering in the main task.

The improvement of dexterity has been achieved developing algorithm for dynamic optimization of the manipulability using redundancy. The results show a significant improvement of manipulability in regions of the workspace close to a singularity. The safety in the shared workspace has been improved by means of human-robot interaction strategies. This work developed and tested an obstacle-avoidance strategy that exploits redundancy to reconfigure the arm of the robot to free space for the medical staff involved in the surgery. Furthermore, this work developed and tested a joint compliance control that allow the surgeon free the workspace pushing the robots arm, besides controlling collision reaction. Moreover, a compliance control is proposed to manually guide the robot, optimizing the setup of the surgery which leads to a reduction of the surgery cost.

All improvements can work together thanks to a hierarchical multi-tasking control that allows to execute the main task simultaneously to the secondary ones without being affected. The different proposed configurations in the control mode allow to modify the behaviour of the robot according to the specific needs of each phase of the surgery.

Finally, the proposed control scheme is integrated into the fetal surgery teleoperation system implementing a software layer into the system control that allows the use of a redundant and collaborative robot.

References

[1] Biere S.S., van Berge Henegouwen M.I., Maas K.W., et al., *Minimally invasive versus open oesophagectomy for patients with oesophageal cancer: a multicentre, open-label, randomised controlled trial*, The Lancet, 2012, vol. 379(9829) pp. 1887-1892.

[2] Hu J.C., Gu X., Lipsitz S.R., et al., *Comparative Effectiveness of Minimally Invasive vs Open Radical Prostatectomy*, JAMA, 2009, vol. 302(14) pp. 1557–1564

[3] Villavicencio A.T., Burneikiene S., Roeca C.M., Nelson E.L. and Mason A., *Minimally invasive versus open transforaminal lumbar interbody fusion*, Surg Neurol Int, 2010, vol. 1 p. 12.

[4] King P.M., Blazeby J.M., Ewings P., Franks P.J., Longman R.J., Kendrick A.H., Kipling R.M. and Kennedy R.H., *Randomized clinical trial comparing laparoscopic and open surgery for colorectal cancer within an enhanced recovery programme*, The British journal of surgery, 2006, vol. 93 pp. 300-308.

[5] Gratacós E., Deprest J., *Current experience with fetoscopy and the Eurofoetus registry for fetoscopic procedures*, Eur J Obstet Gynecol Reprod Biol. 2000, vol. 92(1) pp. 151-159.

[6] Graves C.E., Harrison M.R., and Padilla B.E., *Minimally Invasive Fetal Surgery.*, Clinics in Perinatology, 2017, vol. 44(4), pp. 729–751.

[7] WAPM consensus group on Twin-to-twin transfusion syndrome, Baschat A., Chmait R.H., Deprest J., Gratacós E., Hecher K., Kontopoulos E., Quintero R., Skupski D.W., Valsky D.V. and Ville Y., *Twin-to-twin transfusion syndrome (TTTS)**, Journal of Perinatal Medicine, 2011, 39(2), 107-112

[8] Chalouhi G.E., Essaoui M., Stirnemann J., Quibel T., Deloison B., Salomon L. and Ville Y., *Laser therapy for twin-to-twin transfusion syndrome (TTTS)*, Prenat. Diagn., 2011, vol. 31 pp. 637-646.

[9] Deprest J., Ville Y., Barki G., Hecher K., Gratacos E. and Nicolini U., *Endoscopy in fetal medicine*, Tuttlingen, Germany, 2004, Endopress

[10] Taylor R.H., *A Perspective on Medical Robotics*, Proceedings of the IEEE, 2006, vol. 94(9), pp. 1652-1664

[11] Peters B.S., Armijo P.R., Krause C., Choudhury S.A. and Oleynikov D., *Review of emerging surgical robotic technology*, Surgical Endoscopy, 2018, vol. 32(4), pp. 1636–1655.

[12] Kwoh Y.S., Hou J., Jonckheere E.A. et al., *A robot with improved absolute positioning accuracy for CT guided stereo-tactic brain surgery*, IEEE Trans. Biomed. Eng., 1988, vol. 35(2), pp. 153-160.

[13] Cowley G, *Introducing "Robodoc". A robot finds his calling in the operating room*, Newsweek, 1992, vol 120(21) p. 86.

[14] Davies B.L., Hibber R.D., Ng W.S. ,Timoney A.G., Wickham JE.., *The development of a surgeon robot for prostatectomies*, Proc. Inst. Mech. Eng. H., 1991, vol. 205(1), pp. 35-38.

[15] Harris S.J., Arambula-Cosio F., Mei Q., et al., *The Probot–an active robot for prostate resection*, Proc. Inst. Mech. Eng. H., 1997, vol. 211(4), pp. 317-325.

[16] Unger S.W., Unger H.M., Bass R.T., *AESOP robotic arm*, Surg. Endosc., 1994, vol 8(9), p. 1131

[17] Ballantyne G.H., Moll F., *The da Vinci telerobotic surgical system: the virtual operative field and telepresence surgery*, Surg. Clin. North Am., 2003, vol. 83(6) p. 1239-vii

[18] Hashizume M., Konishi K., Tsutsumi N. Yamaguchi S., Shimabukuro R., *A new era of robotic surgery assisted by a computer-enhanced surgical system*, Surgery, 2002, vol. 131(1 Suppl):S330-S333

[19] Furusho J., Katsuragi T., Kikuchi T., Suzuki T., Tanaka H., Chiba Y., Horio H., *Curved multi-tube systems for fetal blood sampling and treatments of organs like brain and breast*, International Journal of Computer Assisted Radiology and Surgery, 2006, vol.1(Suppl) pp. 223-226

[20] Eisinberg A., Tonet O., Dario P. Macri G., Carrozza M.C., *Development of 6-DOF wire-driven robotic manipulator for minimally invasive fetal surgery*, IEEE International Conference on Robotics and Automation, 2011, pp. 2892-2897

[21] Zhang B., Kobayashi Y., Maeda Y., Chiba T. and Fujie M. G., *Microfabricated instrument for haptic tissue*, International Conference on Biomedical Robotics and Biomechatronics (BioRob), 2006, pp. 1183 - 1188

[22] Dwyer G., *A Continuum Robot and Control Interface for Surgical Assist in Fetoscopic Interventions*, IEEE Robotics and Automation Letters, 2017, vol. 2(3) pp. 1656-1663

[23] Sadda P., Onofrey J. A., Bahtiyar M. O. and Papademetris X., *Better Feature Matching for Placental Panorama Construction*, Lecture Notes in Computer Science, pp. 128–137

[24] Gaisser F., Peeters S. H. P., Lenseigne B., Jonker P., and Oepkes D. , *Stable image registration forin-vivo fetoscopic panorama reconstruction*, Journal of Imaging, vol. 4(1) p 24

[25] Sayols N., et al., *Vision Based Robot Assistance in TTTS Fetal Surgery*, 41st Annual International Conference of the IEEE Engineering in Medicine and Biology Society (EMBC), Germany, 2019, pp. 5855-5861

[26] Khatib O., *A unified approach for motion and force control of robot manipulators: The operational space formulation*, in IEEE Journal on Robotics and Automation, 1987, vol. 3(1) pp. 43-53

[27] Siciliano B., Slotine J.-J. E., *A general framework for managing multiple tasks in highly redundant robotic systems*, Fifth International Conference on Advanced Robotics 'Robots in Unstructured Environments, Pisa, Italy, 1991, vol.2 pp. 1211-1216

[28] Nakamura Y., Hanafusa H. and Yoshikawa T., *Task-Priority Based Redundancy Control of Robot Manipulators*, The International Journal of Robotics Research, 1987, vol. 6(2) pp. 3–15

[29] Ott C., Dietrich A. and Albu-Schäffer A., *Prioritized multi-task compliance control of redundant manipulators*, Automatica, 2015, vol. 53 pp. 416–423.

[30] Sandoval J., Vieyres P., and Poisson G., *Generalized Framework for Control of Redundant Manipulators in Robot-Assisted Minimally Invasive Surgery*, IRBM, 2018, vol. 39(3) pp. 160–166.

[31] Yoshikawa T., *Dynamic manipulability of robot manipulators*, J. Robotics Syst., 1985, vol. 2(1), pp. 113–124.

[32] Chiu S.L., *Control of redundant manipulators for task compatibility*, IEEE Int. Conf. Robotics Autom. (ICRA), Raleigh, 1987, pp. 1718–1724

[33] Maciejewski A.A., Klein C.A., *Obstacle avoidance for kinematically redundant manipulators in dynamically varying environments*, Int. J. Robotics Res., 1985, vol. 4(3) pp. 109-117

[34] Kirćanski M., Vukobratović M., *Trajectory planning for redundant manipulators in presence of obstacles*, 5th CISM-IFToMM Symp. Theor. Pract. Robots Manip., Udine, 1984, pp. 43–58

[35] De Luca A., Ferrajoli L., *Exploiting Robot Redundancy in Collision Detection and Reaction*, IEEE Trans. Robotics Autom., 1998, vol. 14 pp. 566–575

[36] Walker I.D., *The use of kinematic redundancy in reducing impact and contact effects in manipulation*, IEEE Int. Conf. Robotics Autom. (ICRA), Cincinnati, 1990, pp. 434–439

[37] English J.D., Maciejewski A.A., *Fault tolerance for kinematically redundant manipulators: Anticipating free-swinging joint failures*, IEEE/RSJ International Conference on Intelligent Robots and Systems, Nice, 2008, pp. 3299-3305

[38] Kang H. and Wen J. T., *Robotic assistants aid surgeons during minimally invasive procedures*, in IEEE Engineering in Medicine and Biology Magazine, 2001, vol. 20(1) pp. 94-104

[39] Bauzano E., Estebanez B., Garcia-Morales I. and Muñoz V. F., *Collaborative Human–Robot System for HALS Suture Procedures*, in IEEE Systems Journal, 2016, vol. 10(3) pp. 957-966

[40] Su H., Sandoval J., Vieyres P. et al., *Safety-enhanced Collaborative Framework for Tele-operated Minimally Invasive Surgery Using a 7-DoF Torque-controlled Robot*, Int. J. Control Autom. Syst., 2018, vol. 16 pp. 2915–2923

[41] Leporini A., et al., *Technical and Functional Validation of a Teleoperated Multirobots Platform for Minimally Invasive Surgery*, in IEEE Transactions on Medical Robotics and Bionics, 2020, vol. 2(2) pp. 148-156

[42] Markiewicz B.R., *Analysis of the Computed Torque Drive Method and Comparison with Conventional Position Servo for a Computer-controlled Manipulator*, Jet Propulsion Laboratory, Tech. Memo. California Institute of Technology, 1973, pp. 33-601

[43] Middleton R. H. and Goodwin G. C., *Adaptive computed torque control for rigid link manipulations*, Systems and Control Letters, 1988, vol. 10(1) pp. 9–16

[44] Albu-Schaffer A. and Hirzinger G., *Cartesian impedance control techniques for torque controlled light-weight robots*, Proceedings 2002 IEEE International Conference on Robotics and Automation (Cat. No.02CH37292), Washington, DC, USA, 2002, vol.1 pp. 657-663

[45] R. Bischoff et al., *The KUKA-DLR Lightweight Robot arm - a new reference platform for*

robotics research and manufacturing, ISR 2010 (41st International Symposium on Robotics) and ROBOTIK 2010 (6th German Conference on Robotics), Munich, Germany, 2010, pp. 1-8.

[46] *KUKA Fast Research Interface 1.0*, User manual. KUKA Roboter GmbH, 2011.

ETSEIB